

Material Matters™

Volume 10, Number 1

ALDRICH
Materials Science



10th Anniversary Issue

Materials That Matter

CARBON NANOMATERIALS

GRAPHENE NANORIBBONS:

Production and Applications

DRUG DELIVERY POLYMERS

FUNCTIONAL BIOMATERIALS

Synthesized by Double-head
Polymerization Agents

CERAMICS FOR ENERGY APPLICATIONS

ENERGY HARVESTING

Using Lead Zirconium Titanate-based
Ceramic Nanowires

INORGANIC NANOMATERIALS

MAGNETIC NANOPARTICLES

for Cancer Theranostics



Introduction

Welcome to the 10th anniversary issue of *Material Matters*[™]. This issue is focused on the four materials voted by our readers to be the most influential of the past 10 years in the field of materials science—Materials That Matter. During the time that *Material Matters*[™] has been in publication, we have been privileged to have been part of a period of remarkable progress. Research within our field enables an ever-increasing portion of the essential technologies used to solve problems impacting our everyday lives. Materials science provides new materials that enable lightweight, mobile electronics, more highly efficient energy generation and storage, and components, coatings, and delivery vehicles for medical devices and therapeutics, among many others.



Bryce P. Nelson, Ph.D.
Aldrich Materials Science

Ten years ago, the launch of a materials science technical periodical by Sigma-Aldrich helped to define a new direction within the Company by establishing materials science products as unique and independent from those for life scientists, analytical researchers, and synthetic organic chemists. From the start, we focused on our readers (and customers)—the materials researcher. Each issue was to be dedicated to a single materials applications-based theme with topical articles determined and written by leading researchers in the field. Even the title was driven by our readers, who overwhelmingly selected *Material Matters* as the title for the new technical periodical in a poll.

Similarly, the topics for this issue were chosen through an informal poll of researchers conducted to identify the most influential materials during the past 10 years in the field of materials science. Our informal poll received a response from approximately 500 respondents. The results are shown in **Figure 1**. Leading researchers from each of the top four influential research areas were invited to contribute micro-review articles for this issue.

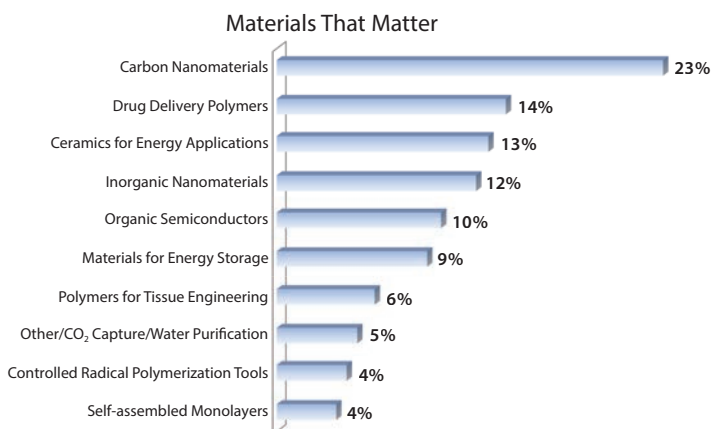


Figure 1. Poll results—"What is the most influential material in the field during the past ten years?"

Carbon nanomaterials outpaced all other material selections by nearly ten percentage points in the poll, followed by polymers for drug delivery, ceramics for energy applications, and inorganic nanomaterials. While many of the most significant new carbon nanomaterials—including fullerenes (1985), carbon nanotubes (1991), and graphene (2004)—were discovered prior to the publication of *Material Matters*[™], the last 10 years has seen an explosion in related research, development, and applications of these innovations. We join our readers in recognizing these materials and celebrate these and other top materials science developments herein.

As always, each article in this publication is accompanied by a list of relevant materials available from Aldrich[®] Materials Science. For additional product information, visit Aldrich Materials Science at aldrich.com/matsci. Please bother us with your new product ideas, as well as thoughts and suggestions for *Material Matters*[™] at matsci@sial.com.

About Our Cover

Materials Science is an interdisciplinary subject, spanning the synthesis and properties of materials, device fabrication, and systems integration. In the past few decades, Materials Science research has seen rapid progress due to its potential to impact modern society with advanced materials in the different areas of biomedical, electronics, and energy. The cover art of this issue showcases a few of the *Material Matters*[™] issues published in the last 10 years with topics of the issues reflecting the progress in the Materials Science field.

Material Matters[™]

Vol. 10, No. 1

Aldrich Materials Science
Sigma-Aldrich Co. LLC
6000 N. Teutonia Ave.
Milwaukee, WI 53209, USA

To Place Orders

Telephone 800-325-3010 (USA)
FAX 800-325-5052 (USA)

International customers, contact your local Sigma-Aldrich office (sigma-aldrich.com/worldwide-offices).

Customer & Technical Services

Customer Inquiries 800-325-3010
Technical Service 800-325-5832
SAFC[®] 800-244-1173
Custom Synthesis 800-244-1173
Flavors & Fragrances 800-227-4563
International 314-771-5765
24-Hour Emergency 314-776-6555
Safety Information sigma-aldrich.com/safetycenter
Website sigma-aldrich.com
Email aldrich@sial.com

Subscriptions

Request your FREE subscription to *Material Matters*:

Phone 800-325-3010 (USA)
Mail Attn: Marketing Communications
Aldrich Chemical Co., Inc
Sigma-Aldrich Co. LLC
P.O. Box 2060
Milwaukee, WI 53201-2060
Website aldrich.com/mm
Email sams-usa@sial.com

Online Versions

Explore previous editions of *Material Matters* aldrich.com/materialmatters



Now available for your iPad[®]
aldrich.com/mm

Material Matters (ISSN 1933-9631) is a publication of Aldrich Chemical Co., Inc. Aldrich is a member of the Sigma-Aldrich Group.

Table of Contents

Articles

Graphene Nanoribbons: Production and Applications	3
Functional Biomaterials Synthesized by Double-head Polymerization Agents	11
Energy Harvesting Using Lead Zirconium Titanate-based Ceramic Nanowires	21
Magnetic Nanoparticles for Cancer Theranostics	29

Featured Products

Graphene and Graphene Nanoribbons	7
A selection of graphene, graphene oxide, and graphene nanoribbons	
Carbon Nanotubes (CNTs)	8
A selection of CNTs and CNT inks	
Nanoclays	9
A list of nanoclays for use in nanocomposites	
Polymerization Agents	15
A selection of ATRP and RAFT polymerization initiators	
Functionalized RAFT and ATRP Polymers	17
A selection of biodegradable, block copolymer, and macro-polymerization agents	
Piezoelectric Materials	25
A list of piezoelectrics of varying particle size and purity	
Nanostructures and Nanomaterials for Energy Applications	25
A selection of nanopowders, nanowires, and nanorods for energy harvesting	
Nanomaterials for Biomedical applications	32
A selection of metallic and oxide-based nanomaterials for biomedical applications	

Your Materials Matter



Josef Zihlmann, Ph.D.
Vice President, Product Management & R&D

We welcome fresh product ideas. Do you have a material or compound you wish to see featured in the Aldrich® Materials Science line? If it is needed to accelerate your research, it matters. Send your suggestion to matsci@sial.com for consideration.

Prof. Mark Hersam of Northwestern University (USA) recommended the addition of inkjet-printable graphene ink (**Aldrich Prod. No. 793663**) to our catalog as a material for printed and flexible electronics. Since graphene ink is based on pristine graphene (as opposed to reduced graphene oxide), it possesses high electrical conductivity, chemical inertness, and mechanical flexibility.¹ This makes it suitable for a range of technologies, including flexible and large-area displays, radio frequency identification tags, portable energy harvesting and storage, biomedical and environmental sensor arrays, and logic circuits. The rheology of this graphene ink can also be tuned to enable printing by other methods, including gravure printing² (**Aldrich Prod. No. 796115**) and screen printing³ (**Aldrich Prod. No. 798983**).

References

- (1) Secor, E. B.; Prabhumirashi, P. L.; Puntambekar, K.; Geier, M. L.; Hersam, M. C. Inkjet Printing of High Conductivity, Flexible Graphene Patterns, *J. Phys. Chem. Lett.* **2013**, *4*, 1347–1351.
- (2) Secor, E. B.; Lim, S.; Zhang, H.; Frisbie, C. D.; Francis, L.; Hersam, M. C. Gravure Printing of Graphene for Large-Area Flexible Electronics, *Adv. Mater.* **2014**, *26*, 453–4538.
- (3) Hyun, W. J.; Secor, E. B.; Hersam, M. C.; Frisbie, C. D.; Francis, L. High-Resolution Patterning of Graphene by Screen Printing with a Silicon Stencil for Highly Flexible Printed Electronics, *Adv. Mater.* **2015**, *27*, 109–115.

Graphene dispersion

conductive ink; inkjetting ink; graphene ink

793663-5ML

5 mL

Have you missed any of our recent issues?

- Vol. 9 No. 4: Materials for Energy Harvesting and Storage (**REO**)
- Vol. 9 No. 3: Polymers in Therapeutics and Nanomedicine (**QZP**)
- Vol. 9 No. 2: Inorganic Materials in Biomedical Applications (**QIV**)
- Vol. 9 No. 1: Materials for Flexible and Printed Electronics (**QFD**)
- Vol. 8 No. 4: Materials for Energy Storage and Efficiency (**PVS**)
- Vol. 8 No. 3: Polymers for Biomedical Engineering (**PQN**)

To view all of our issues or to subscribe to our newsletter, visit aldrich.com/materialmatters

INTRODUCTION TO CARBON NANOMATERIALS



Jia Choi, Product Manager
Aldrich Materials Science

The abundance of new nanomaterial technologies developed within the last ten years has brought great opportunity to electronics, energy, and biomedical research.^{1–3} Carbon-based nanomaterials, in particular, possess extraordinary electrical, thermal, chemical, and mechanical properties that make them unique among these new nanomaterials. Carbon nanomaterials have found applications in diverse areas such as composites, energy storage and conversion, sensors, drug delivery, field emission devices, and nanosized electronic components.^{4–6}

Carbon nanomaterials are a diverse collection that includes zero-dimensional (0D) fullerenes, one-dimensional (1D) carbon nanotubes, and two-dimensional (2D) graphene. All of these materials are allotropes of carbon in well-defined conjugated sp^2 structures (Figure 1).

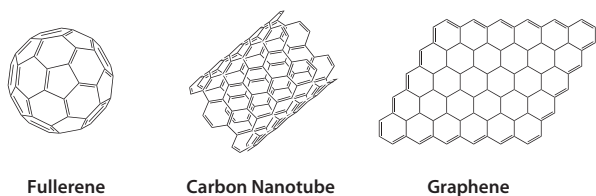


Figure 1. Carbon nanomaterials

Newly developed fullerenes have been used to advance research in the fields of superconductivity, thin films, and supramolecular assembly over the last few years.⁷ Carbon nanotubes continue to gain attention and have impacted many fields; the number of potential applications continues to grow. Research on carbon nanotube chemistry, the control of electronic properties, and the assembly of nanotubes in electronic devices are particularly active areas.⁸

Many remarkable research breakthroughs have been made on graphene since its first isolation by Novoselov, Geim, and co-workers through the

exfoliation of graphite in 2004.⁹ Compared to other carbon nanomaterials, the long-range π -conjugation found in graphene yields extraordinary mechanical strength, exceptionally high electronic and thermal conductivities, and impermeability to gases, as well as many other exceptional properties.¹⁰ However, one fundamental hurdle to the use of graphene in electronic devices has been its lack of a band gap, making devices fabricated using pristine graphene essentially impossible to switch off.¹¹ The introduction of an appreciable band gap into graphene has been identified as the most straightforward way to solve this issue. This has driven research into graphene nanoribbons, which are no longer semi-metallic due to quantum confinement.¹¹

In recognition of the continued rapid advance in carbon nanomaterials research, we have invited Professor James Tour to contribute an article discussing graphene nanoribbons, the latest addition to the carbon nanomaterials “family.” The following article presents an overview of the synthesis of graphene nanoribbons completed through the unzipping of multi-walled carbon nanotubes, as well as a discussion of their potential applications.

References

- (1) De Franceschi, S.; Kouwenhoven, L. Nanotechnology: Electronics and the single atom. *Nature* **2002**, *417*, 701–702.
- (2) Zhang, Q.; Uchaker, E.; Candelaria, S. L.; Cao, G. Nanomaterials for energy conversion and storage. *Chemical Society Reviews* **2013**, *42*, 3127–317.
- (3) Biju, V. Chemical modifications and bioconjugate reactions of nanomaterials for sensing, imaging, drug delivery and therapy. *Chemical Society Reviews* **2014**, *43*, 744–764.
- (4) Dai, L.; Chang, D. W.; Baek, J.-B.; Lu, W. Carbon nanomaterials for advanced energy conversion and storage. *Small* **2012**, *8*, 1130–1166.
- (5) Jariwala, D.; Sangwan, V. K.; Lauhon, L. J.; Marks, T. J.; Hersam, M. C. Carbon nanomaterials for electronics, optoelectronics, photovoltaics, and sensing. *Chemical Society Reviews* **2013**, *42*, 2824–2860.
- (6) Lim, D.-J.; Sim, M.; Oh, L.; Lim, K.; Park, H. Carbon-based drug delivery carriers for cancer therapy. *Archives of Pharmacal Research* **2014**, *37*, 43–52.
- (7) (1) Margadonna, S.; Prassides, K. Recent advances in fullerene superconductivity. *Journal of Solid State Chemistry* **2002**, *168*, 639–652.
(2) Schenning, A. P. H. J.; George, S. J. Phases full of fullerenes. *Nature Chemistry* **2014**, *6*, 658–659.
- (8) (1) Schnorr, J. M.; Swager, T. M. Emerging applications of carbon nanotubes. *Chemistry of Materials* **2011**, *23*, 646–657.
(2) De Volder, M. F. L.; Tawfik, S. H.; Baughman, R. H.; Hart, A. J. Carbon nanotubes: Present and future commercial applications. *Science* **2013**, *339*, 535–539.
- (9) Novoselov, K. S.; Geim, A. K.; Morozov, S. V.; Jiang, D.; Zhang, Y.; Dubonos, S. V.; Grigorieva, I. V.; Firsov, A. A. Electric field effect in atomically thin carbon films. *Science* **2004**, *306*, 666–669.
- (10) Novoselov, K. S.; Fal'ko, V. I.; Colombo, L.; Gellert, P. R.; Schwab, M. G.; Kim, K. A. Roadmap for graphene. *Nature* **2012**, *490*, 192–200.
- (11) Allen, M. J.; Tung, V. C.; Kaner, R. B. Honeycomb carbon: A review of graphene. *Chemical Reviews* **2010**, *110*, 132–145.

GRAPHENE NANORIBBONS: PRODUCTION AND APPLICATIONS



Ayrat M. Dimiev¹ and James M. Tour²

¹EMD Performance Materials Corp., 70 Meister Ave, Somerville, NJ 08876 USA

²Departments of Chemistry, Materials Science and NanoEngineering, and Computer Science, and the Smalley Institute for Nanoscale Science and Technology
Rice University, MS-222, 6100 Main Street, Houston, Texas 77005 USA

Email: tour@rice.edu

Introduction

Graphene is a one-atomic-layer thick two-dimensional material made of carbon atoms arranged in a honeycomb structure. Its fascinating electrical, optical, and mechanical properties ignited enormous interdisciplinary interest from the physics, chemistry, and materials science fields.¹⁻³ The newly discovered properties pave the way to applications in transparent conductive films, electronic and opto-electronic devices, actuators, sensors, composites, and more.

Graphene nanoribbons (GNRs) are narrow strips of graphene. The quasi one-dimensional nature of GNRs results in additional advantages over graphene sheets, the more widely known two-dimensional counterpart to GNRs. For example, the high aspect ratio of GNRs significantly lowers the percolation threshold in conductive films and polymer composites, and renders them suitable for spinning fiber from their liquid crystalline alignment.

Synthesis Methods

The structure and physical properties of GNRs vary significantly depending on the synthesis method—a single term for all GNRs can cause confusion among non-experts because of the resulting structural difference between different types of GNRs. Today, there are three major approaches for fabrication of GNRs: 1) cutting from graphene using lithography; 2) bottom-up synthesis from polycyclic molecules; and 3) unzipping of carbon nanotubes (CNTs). In fact, GNRs produced using those three methods are very different and have little in common.

Lithography

This approach yields single-layer GNRs on a substrate surface. The number of publications on this approach is significant. The use of lithographically produced GNRs is limited to applications where GNRs lie flat on a surface. Bulk quantities cannot be produced using lithographic methods. Also, due to inherent limits in the lateral resolution of lithography-based methods, lithographically produced GNRs have jagged edges.⁴⁻⁶ While this method produces highly precise and very narrow GNRs, the resulting uncontrolled jagged edges make it difficult to control the electronic properties of the resulting materials.

Bottom-Up

The bottom-up fabrication of GNRs involves multi-step organic synthesis based on cyclization of pre-synthesized polymer chains. This method allows for the creation of very narrow ribbons with atomically precise edge configuration.⁷⁻⁹ Until recently, this type of GNRs could only be prepared on the surface of a substrate,^{7,8} limiting the potential for bulk production. Despite the fact that such ribbons have been recently synthesized in a scale of hundreds of milligrams,⁹ it is difficult to see their actual applications in the near future. While the high precision and narrow size distribution resulting from the bottom-up synthesis of GNRs may yield future benefits, there are currently no ready-to-use techniques to further process these tiny structures. This technique has not yet been fully exploited, and it is difficult to envision its actual application in the near future.

Unzipping

The third approach to the fabrication of GNRs is based on the longitudinal opening, or unzipping, of multi-walled carbon nanotubes (MWCNTs).^{10,11} The reported techniques vary, but almost all of them are solution-based processes. The major advantage of this approach over the first two is the potential of mass production on the kilogram scale. Significantly lower cost is another advantage. Also, based on the number of recent publications, it is likely that these CNT-derived GNRs will be the first to find actual applications. Herein, we will review the various aspects of GNRs produced by unzipping of carbon nanotubes as well as their current and emerging applications.

Production of GNRs by Unzipping of Carbon Nanotubes

The Tour group first developed the method used to produce GNRs by longitudinal splitting of carbon nanotubes using potassium (K) vapor and then later in solution using sodium-potassium alloy (Na/K)¹⁰ (Figure 1).

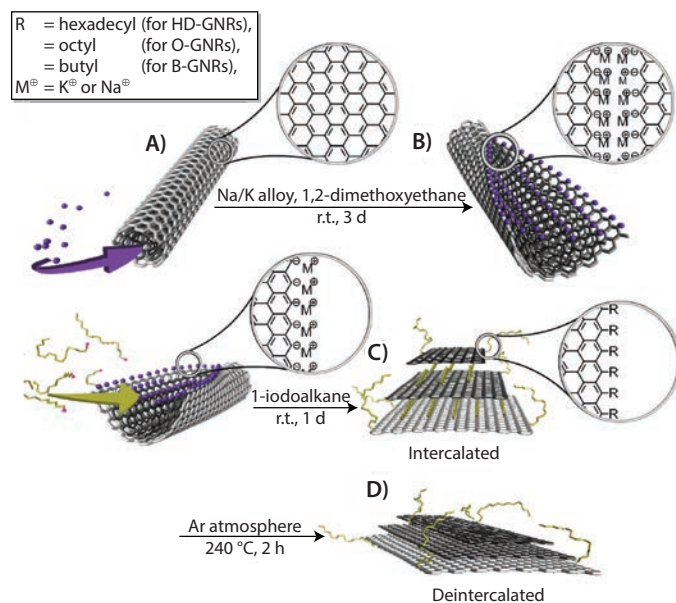


Figure 1. Scheme for unzipping and functionalization of GNRs: (A) intercalation of potassium between the walls of MWCNTs; (B) splitting process of MWCNTs and formation of GNRs with active carboanionic edges (M = K or Na); (C) *in situ* functionalization and intercalation of GNRs with alkyl groups; and (D) deintercalation of functionalized GNRs. Reprinted with permission from ACS Nano, 2012, 6, 4231–4240. Copyright 2012 American Chemical Society.¹⁰

MWCNTs are unzipped via intercalation of the K/Na alloy between the nanotube walls in a 1,2-dimethoxyethane (DME) solvent as shown in Figure 1A. This lattice expansion induces sufficient stress to longitudinally break the nanotube walls. The carbon atoms at the newly formed edges are reduced to their highly reactive carboanionic form (Figure 1B), making them highly susceptible to electrophilic attack. If the intermediate product (Figure 1B) is quenched with methanol, followed by aqueous washing, the metal cations on the edges are replaced with protons. This yields H-terminated GNRs (Aldrich Prod. No. 797774) or simply GNRs. Figure 2 shows MWCNTs fully unzipped after treatment. These GNRs, however, are not completely flat due to van der Waals interaction between the nanotube walls. The GNRs can be completely flattened and partially exfoliated by bath sonication in chlorosulfonic acid.¹¹ The electrical conductivity of the flattened 3.5 to 5 nm thick GNR stacks, comprising 10 to 14 layers, is in the range of 70,000 to 95,000 S/m.¹¹ These values are comparable to the data reported for other graphitic structures.

To prepare alkylated GNRs (alk-GNRs) (HD-GNRs when R=hexadecyl, Aldrich Prod. No. 797766), the intermediate product is exposed to 1-halo-alkanes (Figure 1C). Intercalated potassium is successfully replaced by haloalkanes that predominantly functionalize the edges (and, to some extent, the basal planes) and serve as intercalants in the resulting alk-GNRs. The alk-GNRs bearing long alkyl chains are well-dispersible in organic solvents such as alcohols, ketones, ethers, and alkanes (Figure 3). Particularly stable dispersions are produced in chloroform or chlorobenzene.

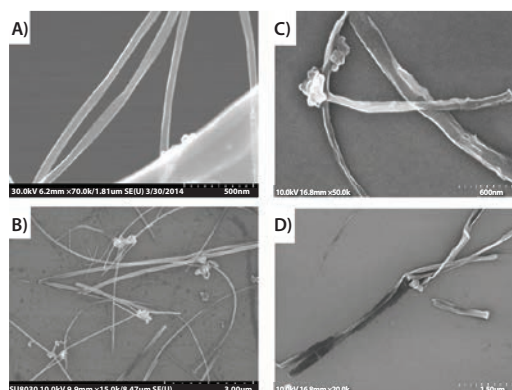


Figure 2. SEM images of (A) and (B) MWCNTs and (C) and (D) fully unzipped MWCNTs.

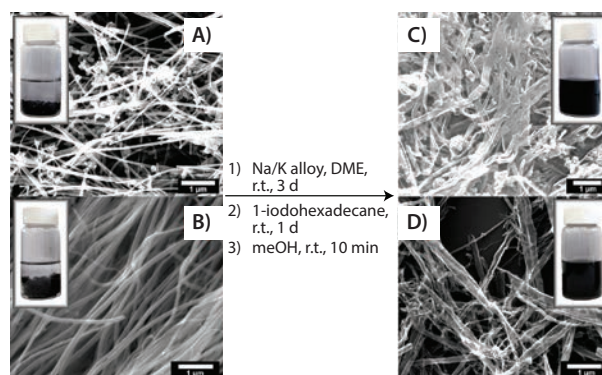


Figure 3. Solubility test. SEM images showing the splitting and functionalizing of commercially available MWCNTs and the photographic difference in solubility between functionalized GNRs and pristine MWCNTs: (A) and (B) two different types of pristine MWCNTs and a 0.1 mg/mL suspension in chloroform; (C) and (D) hexadecylated (HD)-GNRs and a 0.1 mg/mL stable dispersion in chloroform. Reprinted with permission from ACS Nano, 2012, 6, 4231–4240. Copyright 2012 American Chemical Society.¹⁰

Raman spectroscopy (Figure 4) has proven an effective and nondestructive method for the characterization of graphitic carbon nanostructures. The main Raman signals in the spectra of any type of graphitic carbon are the G-band at $\sim 1,680 \text{ cm}^{-1}$ and the 2D-band at $\sim 2,700 \text{ cm}^{-1}$. The D-band at $\sim 1,360 \text{ cm}^{-1}$ is caused by defects serving as photon scattering centers, and it is indicative of the quality of the graphitic structure. Thus, evolution of the D-band during unzipping and functionalization procedures gives valuable information about the nature of as-prepared GNRs. The Raman spectrum of MWCNTs contains only weak D-band signals, suggesting high crystallinity of the parent MWCNTs. In the spectrum of as-produced protonated GNRs, the D-band intensity significantly increases. This is attributed to the carbon atoms on ribbon edges, which act as photon scattering centers. After alkylation, the D-band intensity increases even further, indicating increase in the defect density. We attribute this observation to some covalent functionalization of the GNRs' basal planes. Basal plane alkylation converts the sp^2 carbon atom to the sp^3 carbon atom, thus creating a defect in the otherwise perfect graphene plane. The G/2D ratio for alk-GNRs corresponds to that of a single layer graphene. This suggests separation of GNRs caused by intercalation of alkyl chains between the GNRs.

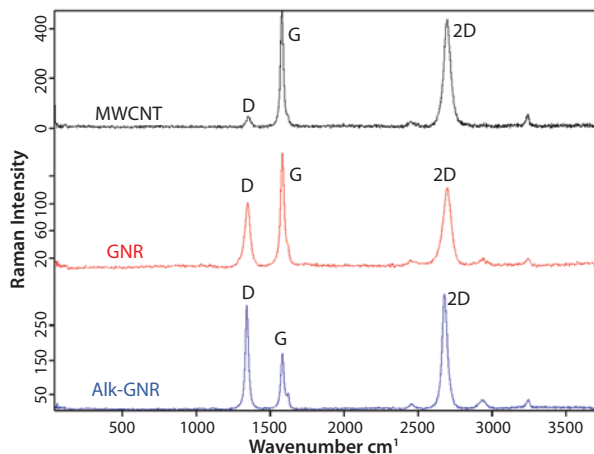


Figure 4. Raman spectra for MWCNTs, GNRs and alk-GNRs.

Potential Applications of GNRs

Both H-terminated GNRs (Aldrich Prod. No. 797774) and alkylated GNRs (Aldrich Prod. No. 797766) have a broad range of potential applications. The most apparent is the incorporation of GNRs in polymer hosts for the fabrication of novel composite materials. GNRs have the same high aspect ratio as their parent MWCNTs, but differences in their nanostructure produce unique and unexpected results. For example, the incorporation of GNRs into a dielectric polymer host dramatically changes its electric properties^{12,13} in a way that is significantly different from that achieved by incorporation of MWCNTs. The most intriguing result is that GNR-containing polymer composites possess remarkably low loss (<0.02) at reasonably high permittivity values (Figure 5). This is important because the miniaturization of electronic components requires materials with high permittivity and low loss in the radio and low microwave frequency region. In the high frequency microwave region, low loss is critical for antennas and other military applications. By varying the type and content of GNRs, the loss and permittivity of composites can be tuned to desirable values over a wide range. The dielectric constant can be tuned from moderate to extremely high (>1,000) values, while the corresponding loss tangent can be varied from ultralow (<0.02) to high (~1.0).¹³

Another promising application of GNRs is as electrode material for batteries and supercapacitors. In one reference,¹⁴ a unique hierarchical structure composite of graphene-wrapped MnO₂-GNRs (GMG) was successfully designed and synthesized (Figures 6 and 7). In this composite, graphene flakes tightly sandwiched nanosized MnO₂ that grew directly on the GNRs.

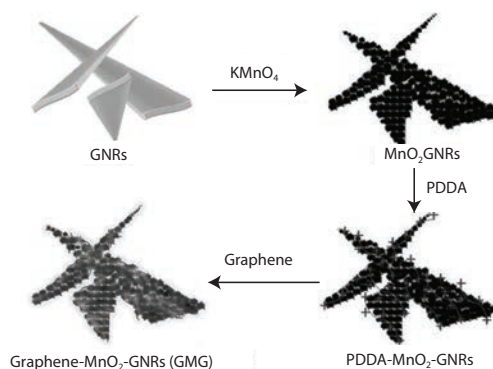


Figure 6. Illustration of the synthesis of the graphene-wrapped MnO₂-GNRs (GMG) composite. Reprinted with permission from Adv. Mater. 2013, 25, 6298–6302. Copyright 2013 John Wiley and Sons.¹⁴

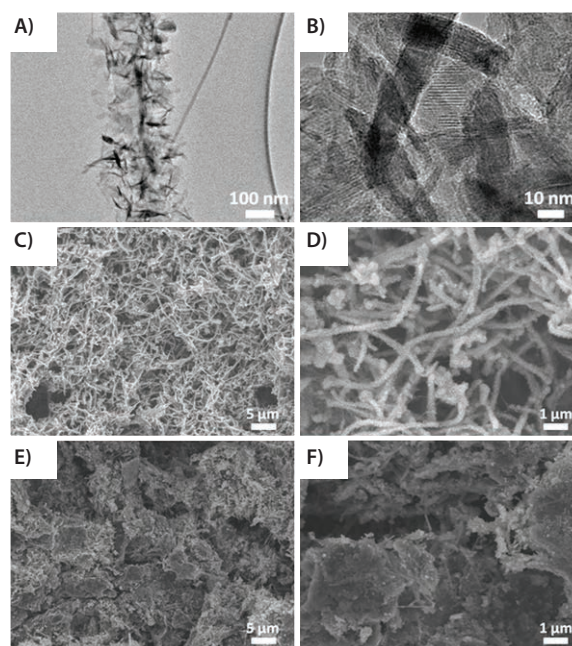


Figure 7. (A) and (B) TEM images of MnO₂-GNRs (MG); (C) and (D) SEM images of MG; and (E) and (F) GMG. Reprinted with permission from Adv. Mater. 2013, 25, 6298–6302. Copyright 2013 John Wiley and Sons.¹⁴

The synthesis of the GMG composite has produced an effective component to improve the electrochemical stability of the electrode materials for lithium-ion batteries.

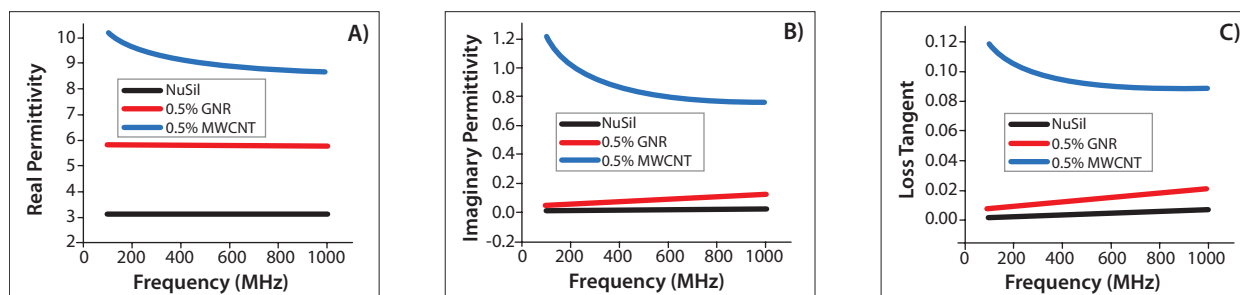


Figure 5. Dielectric properties of the GNR/NuSil (silicon elastomer) composites. (A) Real permittivity, (B) imaginary permittivity, and (C) loss tangent of pure NuSil (black), MWCNT/NuSil (blue), and GNR/NuSil (red) composites containing 0.5 wt % incorporated conductive filler. Reprinted with permission from ACS Appl. Mat. Interf. 3, 4657–4661 (2011). Copyright 2011 American Chemical Society.¹²

Electrochemical experiments demonstrate that the GMG exhibits enhanced specific capacity and improved cycling stability as anode materials compared to MnO_2 -graphene or pure MnO_2 because of the synergistic effect between the graphene, GNRs, and MnO_2 . These characteristics helped achieve stable capacity at several different current densities. For example, the value of specific capacity increased to 890 mAh/g at 180 cycles from 672 mAh/g at 2 cycles in the current density of 0.1 A/g. The rate performance demonstrates that the GMG electrode remained stable after extended rate cycles. For GMG, in the first 5 cycles, the specific capacity decreased as had been seen with MG. After 5 cycles, the value of GMG discharge capacity decreased from 571 mAh/g at 6 cycles to 465 mAh/g at 20 cycles, but then increased to 648 mAh/g at 170 cycles. Even after 250 cycles, the GMG still maintained a specific capacity of 612 mAh/g. Moreover, the Coulombic efficiency of GMG was maintained at over 99%, excluding the first several cycles.

In another work,¹⁵ GNRs were used to fabricate a nanocomposite material of polyaniline (PANI) and GNRs (Figure 8). GNRs were selected as a template on which PANI nanorods were grown. A nanocomposite of PANI-GNRs was prepared by the *in situ* polymerization of aniline in the presence of GNRs. In this composite, GNRs not only serve as the substrate to grow the PANI nanorods and improve the electrical conductivity of the composite, but also increase the effective utilization of PANI and enhance the mechanical property of the composite.

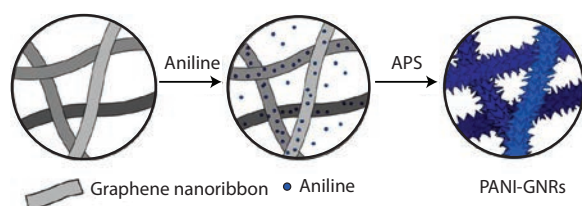


Figure 8. Illustration of the synthesis of the PANI-GNRs composite with PANI polymerized directly on the GNRs using APS (ammonium persulfate). Reprinted with permission from ACS Appl. Mat. Interf. 2013, 5, 6622–6627. Copyright 2013 American Chemical Society.¹⁵

The resulting composite has a high specific capacitance of 340 F/g and stable cycling performance with 90% capacitance retention over 4,200 cycles. The high performance of the composite results from the synergistic combination of electrically conductive GNRs and highly capacitive PANI.

As another potential application, alk-GNRs were used in polymer composites to lower the permeability of gases.¹⁶ A thermoplastic polyurethane (TPU) composite film containing alk-GNRs was produced by solution casting. The HD-GNRs (Aldrich Prod. No. 797766) were well-distributed within the polyurethane matrix, leading to phase separation of the TPU. Nitrogen gas effective diffusivity of TPU was decreased by three orders of magnitude with only 0.5 wt % alk-GNRs (Figure 9).

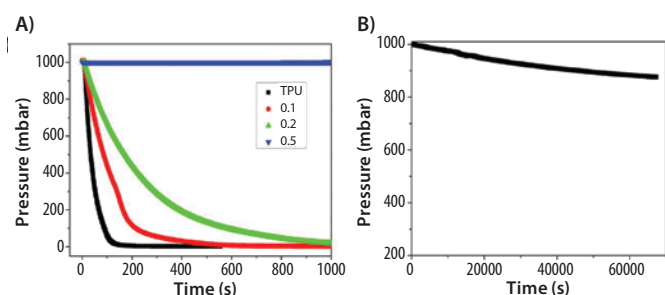


Figure 9. (A) Pressure drop of TPU and TPU/HD-GNRs films with respect to time. (B) Pressure drop of TPU/0.5 wt % HD-GNRs composite film over a longer time period. Reprinted with permission from ACS Appl. Mat. Interf. 2013, 7, 10380–10386. Copyright 2013 American Chemical Society.¹⁶

The incorporation of alk-GNRs also improved the mechanical properties of the composite films, as predicted by the phase separation and indicated by tensile tests and dynamic mechanical analyses. The improved properties of the composite film could lead to potential applications in food packaging and lightweight mobile gas storage containers. As a demonstration for their potential to inhibit gas permeation in Figure 9, see the comparison of efficacies in Table 1.

Table 1. Comparison of different additives to polymer composites for their role as a gas barrier.

Barrier Material	Gas Permeation
GO ¹⁷ (Aldrich Prod. No. 763705, etc)	80x decrease at 3 wt % filler
Nanoclay ¹⁸ (Aldrich Prod. No. 682608, etc.)	14x decrease at 28 wt % filler
HD-GNRs (Aldrich Prod. No. 797766)	1,000x decrease at 0.5 wt % filler

Conclusion

Both GNRs and alk-GNRs have great potential for numerous applications. Currently, the most promising applications are polymer composites and electrode materials for energy storage. It is expected that these diminutive structures will garner increased interest as they become more readily available for researchers and their unique properties become more thoroughly understood.

References

- Geim, A. K.; Novoselov, K. S. The rise of graphene. *Nature Materials* **2007**, *6*, 183–191.
- Geim, A. K. Graphene: status and prospects. *Science* **2009**, *324*, 1530–1534.
- Novoselov, K. S.; Fal'ko, V. I.; Colombo, L.; Gellert, P. R.; Schwab, M. G.; Kim, K. A. Roadmap for graphene. *Nature* **2012**, *490*, 192–200.
- Han, M. Y.; Özyilmaz, B.; Zhang, Y.; Kim, P. Energy band-gap engineering of graphene nanoribbons. *Phys. Rev. Lett.* **2007**, *98*, 206805.
- Wang, X.; Dai, H. Etching and narrowing of graphene from the edges. *Nature Chem.* **2010**, *2*, 661–665.
- Abramova, V.; Slesarev, A.; Tour, J. M. Meniscus-Mask Lithography for Narrow Graphene nanoribbons. *ACS Nano* **2013**, *7*, 6894–6898.
- Long, C.; Hernandez, Y.; Feng, X.; Müllen, K. From nanographene and graphene nanoribbons to sheets: chemical synthesis. *Angew. Chem. Int. Ed.* **2012**, *51*, 7640–7654.
- Cai, J.; Ruffieux, P.; Jaafar, R.; Bieri, M.; Braun, T.; Bankenburg, S.; Muoth, M.; Seitsonen, A. P.; Saleh, M.; Feng, X.; Müllen, K.; Fasel, R. Atomically precise bottom-up fabrication of graphene nanoribbons. *Nature* **2010**, *466*, 470–473.
- Vo, T. H.; Shekhirev, M.; Kunkel, D. A.; Morton, M. D.; Berglund, E.; Kong, L.; Wilson, P. M.; Dowben, P. A.; Enders, A.; Sinitskii, A. Large-scale solution synthesis of narrow graphene nanoribbons. *Nature Comm.* **2014**, DOI: 10.1038/ncomms4189.
- Genorio, B.; Lu, W.; Dimiev, A. M.; Zhu, Y.; Raji, A.-R. O.; Novosel, B.; Alemany, L. B.; Tour, J. M. In situ intercalation replacement and selective functionalization of graphene nanoribbon stacks. *ACS Nano* **2012**, *6*, 4231–4240.
- Kosynkin, D. V.; Lu, W.; Sinitskii, A.; Pera, G.; Sun, Z.; Tour, J. M. Highly conductive graphene nanoribbons by longitudinal splitting of carbon nanotubes by potassium vapor. *ACS Nano* **2011**, *5* (2), 968–974.
- Dimiev, A.; Lu, W.; Zeller, K.; Crowgey, B.; Kempel, L. C.; Tour, J. M. Low Loss, High Permittivity Composites Made from Graphene Nanoribbons. *ACS Appl. Mat. Interfaces* **2011**, *3*, 4657–4661.
- Dimiev, A. M.; Zakhidov, D.; Genorio, B.; Oladimeji, K.; Crowgey, B.; Rothwell, E. J.; Kempel, L. C.; Tour, J. M. Permittivity of dielectric composite materials comprising graphene nanoribbons, The effect of nanostructure. *ACS Appl. Mater. Interfaces* **2013**, *5*, 7567–7573.
- Li, L.; Raji, A.-R. O.; Tour, J. M. Graphene-Wrapped MnO_2 -Graphene Nanoribbons as Anode Materials for high performance lithium batteries. *Adv. Mater.* **2013**, *25*, 6298–6302.
- Li, L. et al. nanocomposite of polyaniline nanorods grown on graphene nanoribbons for highly capacitive pseudocapacitors. *ACS Appl. Mat. Interfaces* **2013**, *5*, 6622–6627.
- Xiang, C. et al. Functionalized low defect graphene nanoribbons and polyurethane film composite for improved gas barrier and mechanical performances. *ACS Nano* **2013**, *7*, 10380–10386.
- Kim, M.; Miura, Y.; Mocosco, C. W. Graphene/polyurethane nanocomposites for improved gas-barrier and electrical conductivity. *Chem. Mater.* **2010**, *22*, 3441–3450.
- Herrera-Alonso, J.; Marand, E.; Little, J. C.; Cox, S. S. Transport properties in polyurethane/clay nanocomposites as barrier materials: Effect of processing conditions. *Membr. Sci.* **2009**, *337*, 208–214.

Graphene and Graphene Nanoribbons

For a complete list of available materials, visit aldrich.com/graphene.

Graphene Nanoribbons

Name	Purity	Dimension	Surface Area	Prod. No.
Graphene nanoribbons	≥90.0% carbon basis, TGA	L x W 2-15 μm x 40-250 nm	BET surf. area 48-58 m ² /g	797774-500MG
Graphene nanoribbons, alkyl functionalized	≥85% carbon basis, TGA	L x W 2-15 μm x 40-250 nm	BET surf. area 38 m ² /g	797766-500MG

Graphene Films

Name	Sheet Resistance	Prod. No.
Monolayer graphene film, 1 cm x 1 cm on copper foil	600 Ω/sq	773697-4EA
Monolayer graphene film, 1 cm x 1 cm on quartz	600 Ω/sq	773719-4EA
Monolayer graphene film, 1 cm x 1 cm on SiO ₂ /Si substrate	600 Ω/sq	773700-4EA
Monolayer graphene film, 1 in. x 1 in. on PET film	700 Ω/sq	745863-1EA 745863-5EA
Monolayer graphene film, 2 in. x 2 in. on PET film	700 Ω/sq	745871-1EA
Suspended monolayer graphene on TEM grid substrate (Quantifoil gold)	170 Ω/sq	798177-1PK

Graphene Inks

Name	Description	Prod. No.
Graphene dispersion	with ethyl cellulose in cyclohexanone and terpineol, inkjet printable	793663-5ML
	with ethyl cellulose in terpineol, gravure printable	796115-10ML
	with ethyl cellulose in terpineol, screen printable	798983-10ML

Graphene Nanoplatelets

Name	Form	Sheet Resistance	Prod. No.
Graphene nanoplatelets	powder	10 (+/-5) Ω/sq (for a 25 μm film)	799084-500MG
	1 mg/mL, dispersion in H ₂ O	10 (+/-5) Ω/sq (for a 25 μm film)	799092-50ML

Graphene Oxide

Name	Description	Form	Prod. No.
Graphene oxide	sheets	flakes	763713-250MG 763713-1G
	2 mg/mL	dispersion in H ₂ O	763705-25ML 763705-100ML
	4 mg/mL	dispersion in H ₂ O	777676-50ML 777676-200ML
	15-20 sheets 4-10% edge-oxidized	powder	796034-1G
	15-20 sheets, 4-10% edge-oxidized, 1 mg/mL in water (dispersion)	liquid	794341-50ML 794341-200ML
	Graphene oxide, ammonia functionalized	1 mg/mL	dispersion in H ₂ O
Reduced graphene oxide	chemically reduced	powder	777684-250MG 777684-500MG

Carbon Nanotubes

For a complete list of available materials, visit aldrich.com/cnt.

Multi-walled Carbon Nanotubes

Production Method	Description	Purity	Prod. No.
CoMoCAT® Catalytic Chemical Vapor Deposition (CVD) Method	O.D. × I.D. × L 10 nm ± 1 nm × 4.5 nm ± 0.5 nm × 3--6 μm (TEM)	≥98% carbon basis	773840-25G 773840-100G
	O.D. × L 6-9 nm × 5 μm diam. 6.6 nm (median) diam. 5.5 nm (mode)	>95% (carbon)	724769-25G 724769-100G
	O.D. × I.D. × L 10 nm × 4.5 nm × 4 μm Aspect ratio (L/D) 350-550 Tubes typically have 6-8 tube walls.	70-80%, TGA (Carbon content)	791431-25G 791431-100G
Catalytic Carbon Vapor Deposition (CCVD) Method	avg. diam. × L 9.5 nm × <1 μm (TEM) thin and short	Metal Oxide <5% TGA	755117-1G
	avg. diam. × L 9.5 nm × 1.5 μm (TEM) thin	Metal Oxide <5% TGA	755133-5G
Chemical Vapor Deposition (CVD) Method	O.D. × L 6-13 nm × 2.5-20 μm 12 nm (average diameter, HRTEM) 10 μm (average length, TEM)	>98% carbon basis	698849-1G
	D × L 110-170 nm × 5-9 μm	>90% carbon basis	659258-2G 659258-10G
Electric Arc Discharge Method	O.D. × L 7-12 nm × 0.5-10 μm powdered cylinder cores	20-30% MWCNT basis	406074-500MG 406074-1G 406074-5G
	O.D. × L 7-15 nm × 0.5-10 μm as-produced cathode deposit	>7.5% MWCNT basis	412988-100MG 412988-2G 412988-10G
Plasma-Enhanced Chemical Vapor Deposition (PECVD) Method	diam. × L 100 nm ± 10% × 30 μm ± 10% vertically aligned on copper wafer substrate	>99.9% carbon basis	687812-1EA
	diam. × L 100-150 nm × 30 μm (SEM) vertically aligned on silicon wafer substrate	>95 atom % carbon basis (x-ray)	687804-1EA

Double-walled Carbon Nanotubes

Production Method	Dimension	Purity	Prod. No.
Catalytic Carbon Vapor Deposition (CCVD) Method	avg. diam. × L 3.5 nm × >3 μm (TEM)	Metal Oxide ≤10% TGA	755141-1G
	avg. diam. × L 3.5 nm × 1-10 μm (TEM)	Metal Oxide <10% TGA	755168-1G
Chemical Vapor Deposition (CVD) Method	O.D. × I.D. × L 5 nm × 1.3-2.0 nm × 50 μm	50-80% carbon basis	637351-250MG 637351-1G

Single-walled Carbon Nanotubes

Production Method	Dimension	Purity	Prod. No.
CoMoCAT® Catalytic Chemical Vapor Deposition (CVD) Method (6,5) chirality; carbon ≥95%	diameter 0.7 - 0.9 nm (by fluorescence)	≥93% (carbon as SWNT)	773735-250MG 773735-1G
CoMoCAT® Catalytic Chemical Vapor Deposition (CVD) Method (6,5) chirality	diameter 0.7 - 0.9 nm (by fluorescence) L ≥700 nm	≥77% (carbon as SWNT)	704148-250MG 704148-1G
CoMoCAT® Catalytic Chemical Vapor Deposition (CVD) Method (7,6) chirality	diameter 0.7 - 1.1 nm L 300-2300 nm (mode: 800nm; AFM)	≥77% (carbon as SWNT)	704121-250MG 704121-1G
CoMoCAT® Catalytic Chemical Vapor Deposition (CVD) method	diameter 0.6 - 1.1 nm	>95% (carbon as SWCNT)	775533-250MG 775533-1G
	diameter 0.7 - 1.4 nm	≥80.0% (carbon as SWNT)	724777-250MG 724777-1G
	diameter 0.7 - 1.3 nm L 450-2300 nm (mode: 800nm; AFM)	≥70% (carbon as SWNT)	704113-250MG 704113-1G
Catalytic Carbon Vapor Deposition (CCVD) Method	average diameter 2 nm × L × 3 (TEM)	>70%, TGA	755710-250MG 755710-1G
Electric Arc Discharge Method	diameter 1.2 - 1.7 nm L 0.3-5 μm	30% (Metallic) 70% (Semiconducting)	750492-100MG
	diameter 1.2 - 1.7 nm L 0.3-5 μm	30% (Metallic) 70% (Semiconducting)	750514-25MG
	diameter 1.2 - 1.7 nm L 0.3-5 μm	2% (Metallic) 98% (Semiconducting)	750522-1MG
	diameter 1.2 - 1.7 nm L 0.3-5 μm	2% (Semiconducting) 98% (Metallic)	750530-1MG
	D × L 2-10 nm × 1-5 μm (bundle dimensions) 1.3-1.5 nm (individual SWNT diameter)	40-60 wt. % carbon basis	698695-1G 698695-5G

Single-walled Carbon Nanotube Inks

Form	SWCNT Concentration	Viscosity	Sheet Resistance	Prod. No.
dispersion in H ₂ O (black liquid)	0.20 +/- 0.01 g/L (by Absorbance at 854 nm)	viscosity ~1.0 mPa.s	<400 Ω/sq (by 4-point probe on prepared film by spray)	791490-25ML 791490-100ML
	1.00 +/- 0.05 g/L (SWCNT concentration by Absorbance at 854 nm)	viscosity 3.0 mPa.s (at 10 sec ⁻¹ shear rate)	<600 Ω/sq (at 85% VLT (ohm/square), by 4-point probe on prepared film by spray)	791504-25ML 791504-100ML
viscous liquid (black)	1 mg/mL	viscosity 17.7 Pa.s at 25 °C (at 10 sec ⁻¹ shear rate)	s<1,000 Ω/sq (by 4-point probe on prepared, at 87.5% VLT (ohm/sq))	792462-25ML 792462-100ML

Nanoclays

For a complete list of available materials, visit aldrich.com/nanoclays.

Name	Additives	Prod. No.
Halloysite nanoclay	-	685445-100G 685445-500G
Nanoclay, hydrophilic bentonite	-	682659-500G
Nanoclay, surface modified	trimethyl stearyl ammonium 25-30 wt. %	682608-500G
	octadecylamine 25-30 wt. %	682616-500G
	dimethyl dialkyl (C14-C18) amine 35-45 wt. %	682624-500G
	aminopropyltriethoxysilane 0.5-5 wt. %; octadecylamine 15-35 wt. %	682632-500G
	methyl dihydroxyethyl hydrogenated tallow ammonium 25-30 wt. %	682640-500G

PRODUCT HIGHLIGHT

Cd-free Quantum Dots

Quantum dots exhibit excellent photoluminescence and electroluminescence properties such as narrow emission bandwidth and high brightness. The toxicity of cadmium makes Cd-free quantum dots more desirable for consumer applications.

Use Cd-free Quantum Dots for these applications:

- LEDs
- Displays
- Solid-state lighting
- Photovoltaics
- Transistors, etc.



Name	Description	Fluorescence Emission (λ _{em})	Prod. No.
InP/ZnS Core-Shell Type Quantum Dots	Kit, 5 x 5 mg/mL in toluene, stabilized with oleylamine ligands	530–650 nm	777285
	5 mg/mL in toluene, stabilized with oleylamine ligands	530 nm	776750
	5 mg/mL in toluene, stabilized with oleylamine ligands	560 nm	776793
	5 mg/mL in toluene, stabilized with oleylamine ligands	590 nm	776769
	5 mg/mL in toluene, stabilized with oleylamine ligands	620 nm	776777
	5 mg/mL in toluene, stabilized with oleylamine ligands	650 nm	776785
PbS Core-type Quantum Dots	Kit, 4 x 10 mg/mL in toluene, oleic acid coated	1,000–1,600 nm	790494
	10 mg/mL in toluene, oleic acid coated	1,000 nm	747017
	10 mg/mL in toluene, oleic acid coated	1,200 nm	747025
	10 mg/mL in toluene, oleic acid coated	1,400 nm	747076
	10 mg/mL in toluene, oleic acid coated	1,600 nm	747084

Learn more about quantum dot properties and applications, including our complete product offering, at aldrich.com/quantumdots

INTRODUCTION TO DRUG DELIVERY POLYMERS



Nicolynn Davis, Product Manager
Aldrich Materials Science

In the past decade advances in science, medicine, and biotechnology have changed the landscape of drug discovery and stimulated the development of highly potent and target-specific drugs. Despite these advances, a significant number of drug candidates fail during preclinical evaluation due to poor efficacy, limited bioavailability, and challenges associated with delivery. Small molecule drugs often suffer from low water solubility, poor stability, short circulation time, and non-specific toxicity limiting their therapeutic efficacy. The development of new biopharmaceuticals such as nucleic acids, peptides, and proteins, has been increasingly successful, accounting for 30% of new drugs brought to market.¹ The therapeutic efficacy of these biopharmaceuticals, however, is limited by low stability and rapid clearance from the body. These challenges, coupled with the complexity of new pharmaceuticals are fueling the evolution of novel drug delivery technologies to overcome bioavailability and delivery obstacles.

The emergence of drug delivery technologies such as polymer-drug conjugates, micelles, nanoparticles, and hydrogels have enabled the development and commercialization of new therapeutic entities. Considerations for the design of drug delivery platforms include the inherent properties of the drug, the desired delivery route, and the required release kinetics. Drug delivery platforms have evolved to include increased control over pharmacokinetic and pharmacodynamics profiles, allow for targeted delivery, and decreased drug toxicity, leading to enhanced efficacy. Controlled drug delivery systems are essential to maintaining sustained drug concentrations in the body, shielding the drug from physiological degradation, and delivering the drug to the desired site of action while minimizing systemic exposure. New highly potent therapeutics can be delivered with dramatically lowered toxicity by encapsulating the active ingredient within a biocompatible carrier. Furthermore, drug delivery platforms can incorporate targeting moieties, such as ligands for biorecognition, or covalently linked polymers such as poly(ethylene glycol) for prolonging blood circulation time improving efficacy and safety.

Polymer science and nanoengineering have revolutionized the central paradigm of drug delivery and have aided in the bench-to-bedside translation of new drug formulations. Synthetic polymers offer a robust and versatile platform for designing novel drug delivery tools to improve drug solubility, decrease toxicity, control release-rates and allow for site-specific delivery. Many of the advances in drug delivery technology

have been inspired by increased control and versatility of polymerization methods to make a synthetic toolbox of polymers for use as drug delivery building blocks. Diversity in the drug delivery toolbox is necessary to facilitate the combination of physical properties from monomers and polymers to make tailor-made block, graft, and other copolymers not otherwise achievable with homopolymers. For example, block copolymers, combine two or more chemically different polymer chains to create hybrid materials that have desirable characteristics not achieved individually. Polymers consisting of hydrophobic and hydrophilic blocks have been successfully used as a drug delivery platform to encapsulate and deliver small molecules and biopharmaceuticals. The structural and physical properties of the polymer blocks dictate drug encapsulation, biocompatibility, and release.

Polymerization techniques, such as ring-opening metathesis (ROMP), nitroxide mediated radical polymerization (NMP), reversible addition-fragmentation chain transfer polymerization (RAFT) and atom transfer radical polymerization (ATRP) enables the creation of highly functional block copolymers and graftable polymers useful for drug delivery. These polymerization techniques allow for precise control over the synthesis process and degree of polymerization, result in low polydispersity, and introduce sequential chemistries to incorporate biochemical signals, targeting moieties, and sites for stealth shielding by PEGylation. Traditional synthesis methods require a multistep process to make functional block copolymers which results in batch-to-batch variability and quality concerns.

In the last decade, specialty monomers and initiators have been developed to streamline polymerization schemes. However, significant challenges in drug delivery remain, including controlling burst release, incorporating stimuli-responsive and on-demand release, and combining multiple drugs with differing properties into a single delivery device. Tackling these highly complex challenges requires innovative drug delivery tools and new materials. Advances in polymer chemistry, with unique initiators and monomers may further the development of novel synthetic polymers capable of incorporating expanded functionality into new drug delivery technologies.

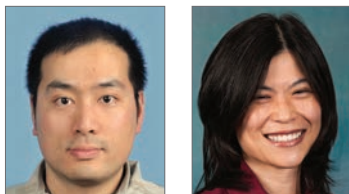
In this anniversary issue, we highlight new polymerization tools, dual double-head initiators, for the preparation of polymers for applications in drug delivery. Double-head agents facilitate simplified polymerization schemes for the preparation of block copolymers. The following review by Hua Wei and Suzie Pun, summarizes recent advancements in double-headed polymerization agents for the synthesis of new well-defined polymeric materials for biomedical applications. The authors illustrate the elegant approach toward advanced material design and development by utilizing double-head agents.

References

- (1) Rader, R. A., FDA pharmaceutical product approvals and trends in 2012, *BioProcess Int.* 11, 2013, 18–27

FUNCTIONAL BIOMATERIALS

SYNTHESIZED BY DOUBLE-HEAD POLYMERIZATION AGENTS

Hua Wei¹ and Suzie H. Pun^{2*}¹Department of Chemistry, Lanzhou University, Lanzhou 730000 China²Department of Bioengineering and Molecular Engineering and Sciences Institute University of Washington, Seattle, Washington 98195 USA

*Email: spun@u.washington.edu

Introduction

Over the past two decades, the rapid advance of controlled living polymerization (CLP) techniques, such as ring-opening polymerization (ROP),¹ nitroxide-mediated polymerization (NMP),² atom transfer free radical polymerization (ATRP),³ and reversible addition-fragmentation chain transfer (RAFT) polymerization,⁴ has enabled synthesis of well-defined polymers with controlled molecular weight and narrow molecular weight distribution (MWD) that are tailor-made for biomedical applications. There is an increasing demand for multifunctional synthetic polymers capable of interacting with, mimicking, or replacing natural materials for use in applications such as drug delivery, molecular imaging, cell therapy, and tissue engineering. One common strategy for the synthesis of multifunctional materials is to combine different synthetic techniques that involve complicated and multistep preparation and purification.⁵ The result, however, is often low reaction yield, batch-to-batch variation, and difficulties in scale-up. Thus, there is considerable need for simplified approaches to synthesis of polymers with advanced architectures and/or bioactive properties. This is particularly important for biomedical applications where simplified synthetic methods are advantageous for scale-up, manufacturing, and FDA approval. Double-head polymerization agents have been developed to meet this demand and provide an elegant and robust approach to achieve this aim. These agents provide a nucleus that integrates different synthetic methods: e.g., CLP,¹⁻⁴ click chemistry,⁶ and thiol chemistry.⁷

Double-head agents, (also called dual, bifunctional, or heterofunctional initiators) contain two functional sites capable of initiating concurrent polymerization independently and selectively. The use of double-head agents offers three advantages over conventional methods for polymer synthesis. The double-head agent: 1) provides an opportunity to prepare block copolymers in a concurrent, one-step manner without the need

for intermediate transformation and protection steps, which is especially useful for the synthesis of block copolymers based on mechanistically incompatible monomers; 2) offers flexibility to the central bridge (block junction) connecting both functional ends that can be customized to meet the requirements for specific applications; and 3) affords two functional termini for the resulting block copolymer.

This review highlights recent progress in this field, with an emphasis on two types of double-head agents with symmetric and asymmetric structures, respectively (Table 1 on the following page). The preparation of polymers using these double-head agents and their biomedical applications are summarized in Figure 1. Finally, a perspective on the future direction of this rapidly developing research field is presented.

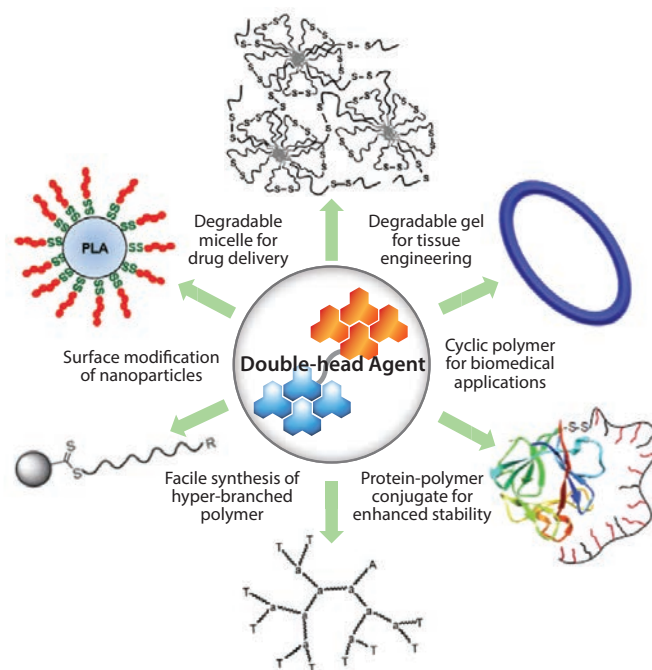
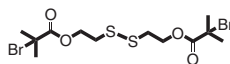
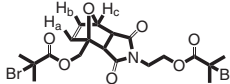
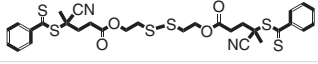
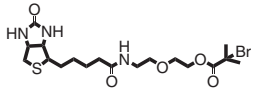
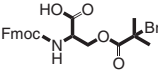
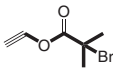
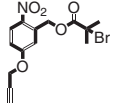
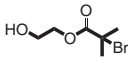
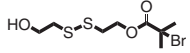
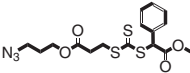
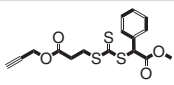
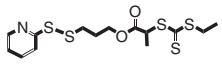
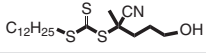
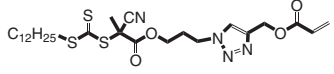
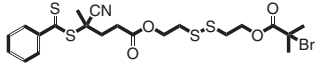


Figure 1. Examples of biomaterials synthesized using double-head agents covered in this review. Adapted with permission from the references as follows: Copyright (2013, 2011, 2008) American Chemical Society;^{20,22,29} Copyright (2006) John Wiley and Sons;⁹ Copyright (2010) Royal Society of Chemistry;²⁵ Copyright (2013) Nature Publishing Group.²⁷

Table 1. Summary of double-head agents with various structures.

Double-head Agent Type	Structure	Ref.
Symmetrical		8,9
		10
		11
Asymmetrical		12
		14
		15
		16
		19,20
		21
		23
		22,24
		25
		26
		27
		28
		29
	30	

Symmetrical Double-head Agents

Symmetrical double-head agents contain the same functional group at each end and are used to initiate simultaneous polymerization from both sides of the agent. These agents have been used to synthesize polymers with internal degradable bridges and also to incorporate functional termini in the cleaved polymer.

Tsarevsky and Matyjaszewski first reported the design of a degradable disulfide-bridged bifunctional ATRP initiator, bis[2-(2-bromopropionyloxy) ethyl] disulfide (BBPrEDS) (Aldrich Prod. No. 723169) for the synthesis of degradable linear polystyrene (PS).⁸ Dithiothreitol (DTT) was used as a reducing agent to break the disulfide bridge and to obtain free thiol-terminated PS with half the molecular weight of the parent polymer.

The BBPrEDS bifunctional initiator was used by Armes and co-workers to synthesize an ABA triblock copolymer by polymerizing first 2-(methacryloyloxy)ethyl phosphorylcholine (MPC) followed by *N*-isopropylacrylamide (NIPAAm), resulting in the PNIPAM₈₀-PMPC₁₂₅-S-S-PMPC₁₂₅-PNIPAM₈₀ ABA triblock copolymer.⁹ This triblock copolymer formed a free-standing gel under physiologically relevant conditions at 37 °C and a copolymer concentration above approximately 8% (w/v). Cleavage of the central disulfide bond by biomolecules such as glutathione caused irreversible dissolution of the micellar gel. These copolymers constitute a new class of injectable gelators that are both biochemically responsive and thermo-responsive and could be useful as depots for localized drug or cell delivery.

Haddleton et al. reported the synthesis of two bifunctional ATRP initiators bearing Diels–Alder adducts—one based on a furan–maleimide adduct and the other based on an anthracene–maleimide adduct—which were used for the synthesis of linear poly(methyl methacrylate) (PMMA).¹⁰ The presence of the Diels–Alder adduct in the middle of the polymer chains allowed for their temperature-modulated reversible cleavage. These “self-healing polymers” can be degraded by heating at high temperature and reformed by heating at lower temperature.

In another example, Zhao's group developed a degradable disulfide-bridged bifunctional RAFT chain transfer agent (CTA), *S*-cyanopentanoic acid dithiobenzoate (S-CPDB).¹¹ In their study, RAFT and ROP were used with S-CPDB to prepare symmetric reduction-responsive amphiphilic star-like terpolymers. Upon redox stimuli and end-group modification, the resulting starlike terpolymers were efficiently converted into thiol-functionalized telechelic stars, degraded miktoarm stars, and comb-like linear multiblock copolymers *via* various thiol modification reactions.

Bis(2-hydroxyethyl)disulfide (HES) (Aldrich Prod. No. 380474) is a degradable disulfide-bridged bifunctional initiator that has been widely used to generate aliphatic polycarbonates by ROP of cyclic carbonates. Zhong et al. prepared poly(ethylene glycol)-*b*-PCL (PEG-SS-PCL) diblock copolymers by first synthesizing biodegradable poly(ϵ -caprolactone) disulfides, PCL-SS-PCL, through ROP of ϵ -caprolactone using HES initiator, reducing the polymers and reacting via disulfide exchange with PEG orthopyridyl disulfide.¹² The reducible PEG-SS-PCL diblock copolymers were used for micellar delivery of the anticancer drug doxorubicin (Dox). Compared to a reduction-insensitive control material, the shell-sheddable micelles released Dox faster in the intracellular environment, resulting in higher anticancer efficacy.

Asymmetrical Double-head Agents

The synthesis of block copolymers based on mechanistically incompatible monomers using asymmetrical double-head agents has attracted considerable attention due to the simplified synthesis and the possibility of a concurrent, one-step process. The hetero double-head agent has two different functional groups that can perform two mechanistically different reactions/polymerizations without intermediate transformation steps. To obtain well-defined block copolymers using this agent via a one-step process, there should be no interactions between the two functional groups, catalysts or initiators, and monomers. In addition, the two polymerizations should proceed in a controlled manner at the same reaction temperature.¹³ Because of these limitations, most of the block copolymers synthesized using hetero double-head agents to date are prepared by a sequential reaction. This section reviews polymers synthesized using asymmetrical double-head agents with an emphasis on materials useful in biomedical applications.

ATRP Initiator-based Double-head Agents

The Maynard group employed a series of ATRP initiator-based double-head agents in an elegant approach to prepare polymer-protein conjugates.¹⁴⁻¹⁶ In one study, a pyridyl disulfide (PDS)-modified ATRP initiator was used to prepare a well-defined poly(2-hydroxyethyl methacrylate) (P(HEMA)) that was then conjugated to bovine serum albumin.¹⁴ In the second report, a biotinylated ATRP initiator was bound to streptavidin and used as a protein macroinitiator for polymerization of NIPAAm.¹⁵ Finally, peptide macroinitiators were synthesized using amino acids with side-chain modified-ATRP initiators in solid-phase peptide synthesis. These macroinitiators were used to synthesize peptide-polymer (e.g., PHEMA and glycopolymers) conjugates exhibiting narrow molecular weight distributions, resulting in well-defined materials.¹⁶

Among the click chemistry group of reactions for facile coupling, the Cu^I-catalyzed azide-alkyne cycloaddition (CuAAC “click”)¹⁷ has received the most attention and has been increasingly employed in polymer functionalization and materials synthesis, especially in conjunction with controlled radical polymerization methods.¹⁸ The CuAAC “click” is particularly well-suited for pairing with ATRP, due to the ease of incorporating clickable functionality into polymers prepared by ATRP and the use of the same catalyst system in each process. The combination of these two powerful techniques has greatly expanded the range of available materials. In one example, the Grayson group used an alkyne-functionalized ATRP initiator to prepare cyclic polymers.¹⁹ Following this methodology, Wei et al. prepared cyclic cationic polymers for nucleic acid delivery and demonstrated that the cyclic polymers were just as effective in gene transfer but less cytotoxic to cultured mammalian cells compared with their linear analogues.²⁰ Another useful agent was prepared by the Gohy and Fustin group; this ATRP initiator contained an *o*-nitrobenzyl ester photocleavable junction and an alkyne group for the CuAAC “click” reaction.²¹

Oh et al. prepared a reducible version of a double-head initiator (HO-SS-iBuBr)²² for integrated ATRP and ROP techniques (HO-iBuBr, [Aldrich Prod. No. 723150](#))²³ introduced by the Matyjaszewski group. In the presence of HO-SS-iBuBr, both ROP of lactide and ATRP of oligo(ethylene glycol) methyl ether methacrylate (OEGMA) were controlled, resulting in well-defined biodegradable block copolymers of PLA-SS-POEGMA with narrow MWD (<1.2). Aqueous micellization of PLA-SS-POEGMA resulted in core/shell micelles with SS links positioned at the interface between PLA cores and POEGMA coronas. In reducing environments such as the cytosol, POEGMA coronas were shed from the PLA cores, causing the precipitation

of PLA core due to the loss of colloidal stability. These results, combined with non-cytotoxicity, indicated that the biodegradable PLA-based sheddable micelles could be useful as novel drug delivery systems for intracellular drug delivery.

Using this same double-head agent, Wei et al. synthesized a ternary, amphiphilic block copolymer PCL-SS-P((GMA-TEPA)-*st*-OEGMA) containing a sheddable hydrophobic PCL block, pH-sensitive oligoamine tetraethylenepentamine (TEPA)-decorated poly(glycidyl methacrylate) (PGMA) block, and a hydrophilic OEGMA segment.²⁴ The sheddable hydrophobic PCL block was synthesized by ROP using the reducible double-head initiator HO-SS-iBuBr and then used as a macroinitiator for subsequent ATRP of GMA and OEGMA. This new block statistical copolymer combines reversible hydrophobization for enhanced particle stability in extracellular environments and statistical hydrophilization for efficient plasmid and siRNA release inside cells. This polymer was shown to be effective for *in vivo* gene transfer to mouse brain due to its multifunctional and bioresponsive properties.

RAFT CTA-based Double-head Agents

RAFT CTA-based double-head agents can be used to generate polymers with reactive termini for a variety of biomedical applications, including protein conjugation, nanoparticle grafting, and biofunctionalization. Zhao's group reported novel strategies for combining RAFT polymerization and CuAAC “click” by using either a Z-azide-functionalized RAFT CTA, S-azidepropoxycarbonyl ethyl S'-methoxycarbonylphenylmethyl trithiocarbonate (AMP)²⁵ or a Z-alkyne-functionalized RAFT CTA²⁶ to prepare homopolymers and multiblock copolymers. These polymers were used for grafting to silica nanoparticles. The Maynard group designed a PDS-functionalized trithiocarbonate CTA for the preparation of protein-polymer conjugates.²⁷ Covalent conjugation of a RAFT-synthesized heparin-mimicking polymer, poly(sodium 4-styrenesulfonate-co-poly(ethylene glycol) methyl ether methacrylate) to basic fibroblast growth factor (bFGF) significantly enhanced protein stability under a variety of environmentally and therapeutically relevant stressors—such as heat, mild and harsh acidic conditions, storage and proteolytic degradation—different from native bFGF.

Advanced polymer structures also can be prepared using RAFT CTA-based double-head agents. Youk and co-workers synthesized well-defined block copolymers using 4-cyano-4-(dodecylsulfanylthiocarbonyl) sulfanylpentanol (CDP) as a dual initiator for RAFT polymerization and ROP in a one-step process.²⁸ In one example, block copolymers with one block synthesized by RAFT polymerization of vinyl monomers and a second block synthesized by ROP of cyclic monomers were prepared in a one-step synthesis with selective catalysts for ROP that did not interfere with RAFT polymerization. RAFT polymerization in the presence of a compound capable of both reversible chain transfer through a thiocarbonylthio moiety and propagation via a vinyl group leads to highly branched copolymers. Sumerlin et al. synthesized an acryloyl trithiocarbonate and performed copolymerization with NIPAAm in ratios selected to control the distribution and length of branches in the resulting thermo-responsive copolymers.²⁹ Retention of the active thiocarbonylthio compound during the polymerization was evidenced by a successfully subsequent chain extension of the resulting branched PNIPAAm macro-CTA by a further RAFT polymerization of a second monomer. This approach could be extendable to the synthesis of a variety of branched stimuli-responsive copolymers with a high concentration of sulfur-containing end groups that can facilitate polyvalent bioconjugation or surface immobilization.

RAFT-ATRP Double-head Agents

Wei et al. introduced a reducible RAFT-ATRP double-head agent for the synthesis of peptide-functionalized copolymers with sheddable shielding blocks for nucleic acid delivery applications.³⁰ An optimized reduction-responsive cationic block copolymer, P(OEGMA)-SS-P(GMA-TEPA), was synthesized using this double-head agent by a combination of RAFT polymerization of OEGMA and ATRP of glycidyl methacrylate (GMA), followed by post-polymerization decoration of reactive epoxy groups in the P(GMA) block by tetraethylenepentamine (TEPA). The resulting diblock copolymer showed well-controlled composition with narrow MWD and was easily modified with a neuron targeting peptide, Tet1, at the outer corona by a Michael-type addition to the free thiols generated by aminolysis of the dithioester end group. The final polymer formed salt-stable particles amenable for *in vivo* use while maintaining high transfection efficiency, likely due to its multifunctional capabilities of targeting, endosomal escape, and deshielding and cargo release endowed by the Tet1 peptide, protonable TEPA amines, and reducible backbone structure, respectively (Figure 2). Thus, due to the combined properties of targeting and shielding, this block copolymer was shown to retain high transfection efficiencies comparable to the analogous homopolymer vectors for targeted gene delivery. The RAFT-ATRP double-head agent, therefore, provides a versatile means for preparing various types of multifunctional drug and gene delivery vehicles.

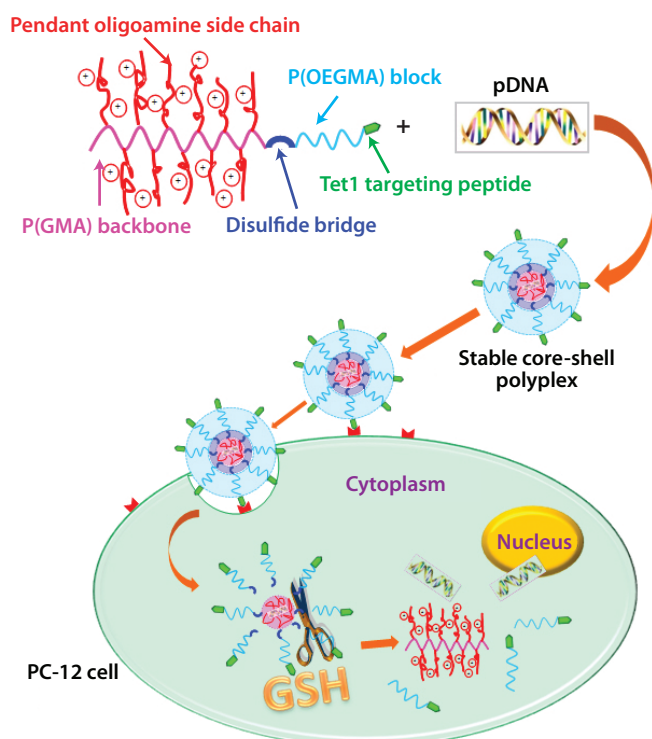


Figure 2. Illustration for P(OEGMA)₁₅-SS-P(GMA-TEPA)₅₀ cationic polymer, DNA condensation, cell binding, endocytosis, and proposed route for subsequent reduction-triggered intracellular unpackage of pDNA. Copyright (2012) American Chemical Society.³⁰

Conclusion and Perspective

The design and development of various double-head agents represent an elegant approach toward advanced materials design. With double-head agents, different polymerizations/reactions can be carried out without intermediate transformation and functionalization steps, sometimes even in a concurrent manner, significantly simplifying the traditional techniques for the preparation of block copolymers as well as generating a broad spectrum of novel block copolymers with fascinating properties based on diverse monomers. It is not surprising that the last decade has seen a tremendous growth in the development of such agents.

It is worth noting that the disulfide bond has attracted most of the attention, and it has been repeatedly employed as the degradable link in a double-head agent due to the excellent compatibility of disulfide with CLP processes, the reversible degradation and formation of the disulfide bond under mild conditions, and also the biological relevance of disulfides. Future research concerning the use of other stimuli-responsive links, such as acidic pH, temperature, enzyme-responsive substrates, and photo-sensitive bridges for the preparation of degradable double-head agents will be a hot topic and remains to be explored.

Looking to the future, much exciting work is expected to develop in the new field of advanced biomaterials prepared using various double-head agents.

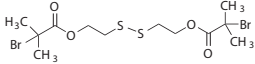
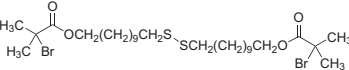
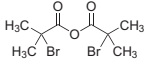
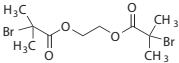
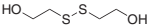
References

- Feng, J.; Zhuo, R. X.; Zhang, X. Z. *Progress in Polymer Science* **2012**, *37*, 211–236.
- Nicolas, J.; Guillauneuf, Y.; Lefay, C.; Bertin, D.; Gigmes, D.; Charleux B. *Progress in Polymer Science* **2012**, *38*, 63–235.
- Sieglwart, D. J.; Oh, J. K.; Matyjaszewski, K. *Progress in Polymer Science* **2012**, *37*, 18–37.
- Gregory, A.; Stenzel, M. H. *Progress in Polymer Science* **2012**, *37*, 38–105.
- Chen, J. C.; Liu, M. Z.; Gong, H. H.; Cui, G. J.; Lv, S. Y.; Gao, C. M.; Huang, F.; Chen, T. T.; Zhang, X. Y.; Liu, Z. *Polymer Chemistry* **2013**, *4*, 1815–1825.
- Such, G. K.; Johnston, A. P. R.; Liang, K.; Caruso, F. *Progress in Polymer Science* **2012**, *37*, 985–1003.
- Roth, P. J.; Boyer, C.; Lowe, A. B.; Davis, T. P. *Macromolecular Rapid Communications* **2011**, *32*, 1123–1143.
- Tsarevsky, N. V.; Matyjaszewski, K. *Macromolecules* **2002**, *35*, 9009–9014.
- Li, C.; Madsen, J.; Armes, S. P.; Lewis, A. L. *Angewandte Chemie International Edition* **2006**, *45*, 3510–3513.
- Syrett, J. A.; Mantovani, G.; Barton, W. R. S.; Price, D.; Haddleton, D. M. *Polymer Chemistry* **2010**, *1*, 102–106.
- Jiang, X.; Zhang, M. J.; Li, S. X.; Shao, W.; Zhao, Y. L. *Chemical Communications* **2012**, *48*, 9906–9908.
- Sun, H. L.; Guo, B. N.; Cheng, R.; Meng, F. H.; Liu, H. Y.; Zhong, Z. Y. *Biomaterials* **2009**, *30*, 6358–6366.
- Bernaerts, K. V.; Prez, F. E. D. *Progress in Polymer Science* **2006**, *31*, 671–722.
- Bontempo, D.; Heredia, K. L.; Fish, B. A.; Maynard, H. D. *Journal of the American Chemical Society* **2004**, *126*, 15372–15373.
- Bontempo, D.; Maynard, H. D. *Journal of the American Chemical Society* **2005**, *127*, 6508–6509.
- Broyer, R. M.; Quaker, G. M.; Maynard, H. D. *Journal of the American Chemical Society* **2008**, *130*, 1041–1047.
- Kolb, H. C.; Finn, M. G.; Sharpless, K. B. *Angewandte Chemie International Edition* **2001**, *40*, 2004–2021.
- Barner-Kowollik, C.; Du Prez, F. E.; Espeel, P.; Hawker, C. J.; Junkers, T.; Schlaad, H.; Van Camp, W. *Angewandte Chemie International Edition* **2011**, *50*, 60–62.
- Laurent, B. A.; Grayson, S. M. *Journal of the American Chemical Society* **2006**, *128*, 4238–4239.
- Wei, H.; Chu, D. S. H.; Zhao, J.; Pahang, J. A.; Pun, S. H. *ACS Macro Letters* **2013**, *2*, 1047–1050.
- Schumers, J. M.; Gohy, J. F.; Fustin, C. A. *Polymer Chemistry* **2010**, *1*, 161–163.
- Sourkahi, B. K.; Cunningham, A.; Zhang, Q.; Oh, J. K. *Biomacromolecules* **2011**, *12*, 3819–3825.
- Jakubowski, W.; Lutz, J. F.; Slomkowski, S.; Matyjaszewski, K. *Journal of Polymer Science, Part A: Polymer Chemistry* **2005**, *43*, 1498–1510.
- Wei, H.; Volpatti, L. R.; Sellers, D. L.; Maris, D. O.; Andrews, I. W.; Hemphill, A. S.; Chan, L. W.; Chu, D. S. H.; Horner, P. J. Pun, S. H. *Angewandte Chemie International Edition* **2013**, *52*, 5377–5381.
- Huang, Y. K.; Hou, T. T.; Cao, X. Q.; Perrier, S.; Zhao, Y. L. *Polymer Chemistry* **2010**, *1*, 1615–1623.
- Zhao, G. D.; Zhang, P. P.; Zhang, C. B.; Zhao, Y. L. *Polymer Chemistry* **2012**, *3*, 1803–1812.
- Nguyen, T. H.; Kim, S. H.; Decker, C. G.; Wong, D. Y.; Loo, J. A.; Maynard, H. D. *Nature Chemistry* **2013**, *5*, 221–227.
- Kang, H. U.; Yu, Y. C.; Shin, S. J.; Youk, J. H. *Journal of Polymer Science, Part A: Polymer Chemistry* **2013**, *51*, 774–779.
- Vogt, A. P.; Sumerlin, B. S. *Macromolecules* **2008**, *41*, 7368–7373.
- Wei, H.; Schellinger, J. G.; Chu, D. S. H.; Pun, S. H. *Journal of the American Chemical Society* **2012**, *134*, 16554–16557.

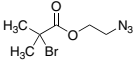
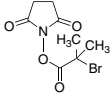
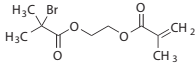
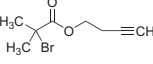
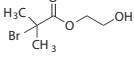
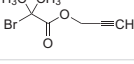
ATRP Initiators

For more information on this product line, visit aldrich.com/polyinitiator.

Symmetric Difunctional Initiators

Name	Structure	Description	Prod. No.
Bis[2-(2-bromoisobutyryloxy)ethyl] disulfide		Atom Transfer Radical Polymerization (ATRP) initiator for the preparation of biodegradable polymers as well as polymers that adhere to gold surfaces. May also be used to introduce a temperature and light sensitive cleavable region into the polymer.	723169-1G 723169-5G
Bis[2-(2-bromoisobutyryloxy)undecyl] disulfide		Atom transfer Radical Polymerization (ATRP) initiator commonly used to functionalize noble metal surfaces, and in the preparation of polymer brushes and biodegradable hydrogels. Also may be used to introduce a temperature and light sensitive cleavable region into the polymer.	733350-500MG
2-Bromoisobutyric anhydride		Highly effective difunctional initiator for atom transfer radical polymerization (ATRP).	766399-1G 766399-5G
Ethylene bis(2-bromoisobutyrate)		Atom Transfer Radical Polymerization (ATRP) initiator for the creation of difunctional polymers. Polymerization will occur at two sites creating a polymer with ester functionality at the center.	723177-1G 723177-5G
2-Hydroxyethyl disulfide		Degradable disulfide-bridged bifunctional initiator.	380474-50ML 380474-250ML

Asymmetric Difunctional Initiators

Name	Structure	Description	Prod. No.
2-Azidoethyl 2-bromoisobutyrate		Bifunctional initiator with a bromoisobutyryl moiety for atom transfer radical polymerization (ATRP) and an azide moiety that can be used in Cu-mediated ligation ("click" chemistry) for biomaterials, carbon nanotubes and graphene sheets.	792055-1G
2-Bromoisobutanoic acid N-hydroxysuccinimide ester		Atom transfer radical polymerization (ATRP) initiator with an NHS ester moiety for conjugation chemistry, useful for biological ligations.	792047-1G
2-(2-Bromoisobutyryloxy)ethyl methacrylate		Atom Transfer Radical Polymerization (ATRP) initiator with a methacrylate functionality for branched polymerization, orthogonal polymerization, or other functionalization.	734586-1G 734586-5G
3-Butynyl 2-bromoisobutyrate		Atom Transfer Radical Polymerization (ATRP) initiator with alkyne functionality. Alkyne can be useful in coupling reactions/ligation.	765104-1G
2-Hydroxyethyl 2-bromoisobutyrate		Atom Transfer Radical Polymerization (ATRP) initiator for the creation of hydroxy functionalized telechelic polymers. Can be used to modify carboxylate- or isocyanate- modified surfaces, particles or biomolecules.	723150-1G 723150-5G
Propargyl 2-bromoisobutyrate		Atom transfer radical polymerization (ATRP) initiator with an acetylene functionality that enables Cu-mediated ligation ("click" chemistry) or other functionalization.	773468-1G

Standard ATRP Initiators

Name	Structure	Description	Prod. No.
Pentaerythritol tetrakis(2-bromoisobutyrate)		Atom Transfer Radical Polymerization (ATRP) initiator for the creation of tetrafunctional polymers. Polymerization will occur at four sites creating a four-arm star polymer.	723193-1G 723193-5G
Poly(ethylene glycol) bis(2-bromoisobutyrate), 2,200		Poly(ethylene glycol)-containing ATRP initiator for generating a triblock copolymer with a PEG block in the center.	741019-1G
Poly(ethylene glycol) methyl ether 2-bromoisobutyrate, 1,200		Poly(ethylene glycol)-containing ATRP initiator for generating a block copolymer with a PEG block on one end. The PEG block is terminated with an unreactive methoxy group.	739456-1G 739456-5G
Poly(ethylene glycol) methyl ether 2-bromoisobutyrate, 2,000		Poly(ethylene glycol)-containing ATRP initiator for generating a block copolymer with a PEG block on one end. The PEG block is terminated with an unreactive methoxy group.	750069-1G 750069-5G
Poly(ethylene glycol) methyl ether 2-bromoisobutyrate, 5,000		Poly(ethylene glycol)-containing ATRP initiator for generating a block copolymer with a PEG block on one end. The PEG block is terminated with an unreactive methoxy group.	736333-1G 736333-5G

RAFT Initiators

For more information on this product line, visit aldrich.com/polyinitiator.

Name	Structure	Description	Prod. No.
4-Cyano-4-[(dodecylsulfanylthiocarbonyl)sulfanyl]pentanoic acid		RAFT agent for controlled radical polymerization; especially suited for the polymerization of methacrylate, methacrylamide and styrene monomers.	723274-1G 723274-5G
Cyanomethyl dodecyl trithiocarbonate		RAFT agent for controlled radical polymerization; especially suited for the polymerization of styrene, acrylate and acrylamide monomers.	723029-1G 723029-5G
Cyanomethyl methyl(phenyl)carbamodithioate		RAFT agent for controlled radical polymerization; especially suited for the polymerization of vinyl ester and vinyl amide monomers.	723002-1G 723002-5G
4-Cyano-4-(phenylcarbonothioylthio)pentanoic acid		RAFT agent for controlled radical polymerization; especially suited for the polymerization of methacrylate and methacrylamide monomers.	722995-1G 722995-5G
2-Cyano-2-propyl benzodithioate		RAFT agent for controlled radical polymerization; especially suited for the polymerization of methacrylate and methacrylamide monomers.	722987-1G 722987-5G
2-Cyano-2-propyl dodecyl trithiocarbonate		RAFT agent for controlled radical polymerization; especially suited for the polymerization of methacrylate, methacrylamide and styrene monomers.	723037-1G 723037-5G
S,S-Dibenzyl trithiocarbonate		Trithiocarbonate-based RAFT agent used as a bifunctional in RAFT polymerization of block copolymers for drug delivery. Provides good control of polymerization of vinyl monomers, including styrene, methacrylate, and acrylamide.	746304-1G 746304-5G
2-(Dodecylthiocarbonothioylthio)-2-methylpropionic acid		RAFT agent for controlled radical polymerization; especially suited for the polymerization of styrene, acrylate and acrylamide monomers.	723010-1G 723010-5G
2-(Dodecylthiocarbonothioylthio)-2-methylpropionic acid N-hydroxysuccinimide ester		Functionalized RAFT agent for controlled radical polymerization; especially suited for the polymerization of styrene; acrylate and acrylamide monomers. NHS ester terminus can be used to conjugate to a variety of biomolecules.	741035-1G 741035-5G
2-Phenyl-2-propyl benzodithioate		RAFT agent for controlled radical polymerization; especially suited for the polymerization of methacrylates/methacrylamides, and to a lesser extent acrylates/acrylamides and styrenes;	731269-1G 731269-5G
Poly(ethylene glycol) methyl ether (4-cyano-4-pentanoate dodecyl trithiocarbonate), 5,400		RAFT agent for controlled radical polymerization; especially suited for the polymerization of styrene, acrylate, and acrylamide monomers to make lithographically and biologically important PEG-block copolymers.	751626-1G 751626-5G
Poly(ethylene glycol) methyl ether (2-methyl-2-propionic acid dodecyl trithiocarbonate), 10,000		RAFT agent for controlled radical polymerization; especially suited for the polymerization of styrene; acrylate; and acrylamide monomers to make lithographically and biologically important PEG-block copolymers.	752495-1G

Functionalized RAFT and ATRP Polymers

For more information on this product line, visit aldrich.com/polymers.

Poly(lactide) Functionalized Polymers

Name	Structure	Molecular Weight	PDI	Prod. No.
Poly(L-lactide), 2-bromoisobutyryl terminated		average M_n 3,000	≤ 1.1 PDI	773247-1G
Poly(D,L-lactide), 4-cyano-4-[(dodecylsulfanyl-thiocarbonyl)sulfanyl]pentonate terminated		average M_n 5,000	≤ 1.5 PDI	792020-1G

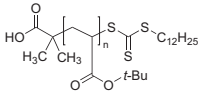
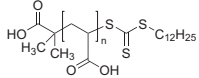
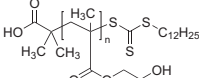
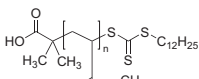
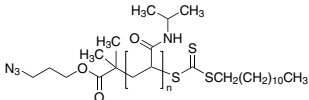
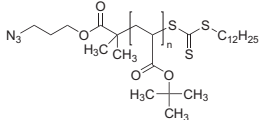
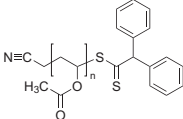
Polystyrene Block Copolymers

Name	Structure	Molecular Weight	PDI	Prod. No.
Polystyrene- <i>block</i> -poly(acrylic acid)		M_n 27,000-31,000 (polystyrene) M_n 4,000-6,000 (poly(acrylic acid)) M_n 31,000-37,000 (total)	≤ 1.1 PDI	746991-1G
Poly(styrene)- <i>block</i> -poly(acrylic acid)		M_n 27,000-31,000 (polystyrene) M_n 1,000-2,000 (poly(acrylic acid)) M_n 28,000-33,000 (total)	≤ 1.1 PDI	747009-500MG
		M_n 27,000-31,000 (polystyrene) M_n 8,000-10,000 (poly(acrylic acid)) M_n 35,000-41,000 (total)	≤ 1.1 PDI	746983-500MG
Polystyrene- <i>block</i> -poly(<i>tert</i> -butyl acrylate), DDMAT terminated, acid terminated		average M_n 12,000	≤ 1.2 PDI	776432-1G

Macro-polymerization Agents

Name	Structure	Molecular Weight	PDI	Prod. No.
Polystyrene, azide terminated		average M_n 15,000	≤ 1.3 PDI	746916-1G
Polystyrene, DDMAT terminated		average M_n 5,000	< 1.1 PDI	772577-1G
		average M_n 10,000	≤ 1.1 PDI	772569-1G
Polystyrene, thiol terminated		average M_n 5,000	≤ 1.1 PDI	746924-1G
		average M_n 11,000	≤ 1.1 PDI	746932-1G

Macro-polymerization Agents (cont'd)

Name	Structure	Molecular Weight	PDI	Prod. No.
Poly(<i>tert</i> -butyl acrylate), DDMAT terminated		average M_n 7,000	< 1.2 PDI	772550-1G
Poly(acrylic acid), DDMAT terminated		average M_n 10,000	≤ 1.1 PDI	775843-1G
Poly(hydroxyethyl methacrylate), DDMAT terminated		average M_n 7,000	< 1.2 PDI	772542-1G
Poly(<i>N,N</i> -dimethylacrylamide), DDMAT terminated		average M_n 10,000	≤ 1.1 PDI	773638-1G
Poly(<i>N</i> -isopropylacrylamide), azide terminated		average M_n 15,000	≤ 1.3 PDI	747068-1G 747068-5G
Poly(<i>tert</i> -butyl acrylate), DDMAT terminated, azide terminated		average M_n 7,000	≤ 1.2 PDI	776424-1G
Poly(vinyl acetate), cyanomethyl diphenylcarbomodithioate		average M_n 5,000	< 1.2 PDI	773328-1G

GRAPHENE

– THE WONDER MATERIAL



SYNTHESIS | ELECTRONICS | ENERGY | COMPOSITES | BIOMEDICAL

FAST-TRACK YOUR GRAPHENE RESEARCH

- Graphene films
- Graphene inks for flexible electronics
- Graphene nanoribbons
- Graphene oxide
- Reduced graphene oxide
- Engineered metals and alloys
- Nanopowders and dispersions
- Electrode and electrolyte materials

For more information on materials for graphene technologies, visit aldrich.com/graphenetech

INTRODUCTION TO CERAMICS FOR ENERGY APPLICATIONS



Niraj Singh, Product Manager
Aldrich Materials Science

Ceramics have drawn significant attention in last ten years as they find expanding applications in energy conversion and storage.¹⁻³ In particular, ceramics have emerged as an important class of materials for use in energy conversion and storage technology and are being developed to help cut carbon dioxide emission. For example, ceramics are used in alternative energy generation technologies such as solid oxide fuel cells, photovoltaics, thermal and vibrational energy harvesting.³⁻⁵ They also find applications as both electrodes and electrolytes in energy storage devices and, thus, have become an essential technology component for the creation of cleaner and more sustainable energy sources.^{3,6} **Figure 1** shows the electrochemical properties of TiO₂ ceramic nanotube array used as electrode material in lithium-ion batteries as a representative.

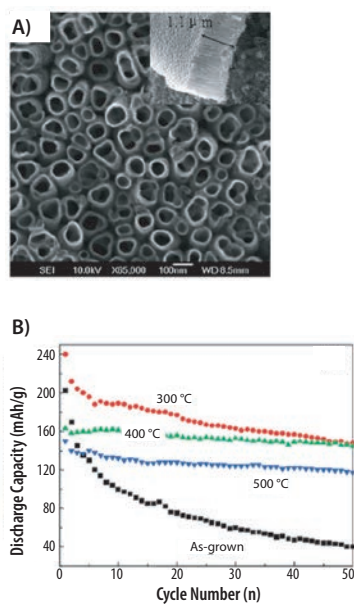


Figure 1. A) SEM image of a TiO₂ nanotube array and B) the dependence of discharge capacity cyclic stability on annealing temperature of the array.⁷

Among these alternative energy technologies, vibrational energy scavenging technology has recently attracted significant attention.⁸ Vibrational energy harvesters typically consist of magnetostrictive or piezoelectric materials. In harvesters based on magnetostrictive properties, mechanical vibrations produce changes in magnetization that are transformed into an electrical current with the help of pick-up coils. Piezoelectric based harvesters generate electric signals produced by vibration-induced charge separation. Ceramic nanowires are one dimensional structures that offer efficient transport of charge and thereby lead to high energy conversion efficiency in piezoelectric nanowires based energy harvesters. Nanowires of ceramics such as barium titanate, lead zirconium titanate, and zinc oxide are well known for their outstanding piezoelectric properties.

In the next article, "Energy harvesting using lead zirconium titanate-based ceramic nanowires," Prof. Henry Sodano (University of Florida, Gainesville, USA) reports on the fabrication and testing of an ambient mechanical vibrational energy harvester using lead zirconium titanate (PZT)-based ceramic nanowires. It has been demonstrated that the PZT-based nanowires with composition near the morphotropic phase boundary show high piezoelectric coupling coefficient and high power density and are useful for sensing and energy harvesting applications.

References

- (1) Cao, F.; McEnaney, K.; Chen, G.; Ren, Z. *Energy Environ. Sci.* **2014**, *7*, 1615.
- (2) Matiko, J. W.; Grabham, N. J.; Beeby, S. P.; Tudor, M. J. *Meas. Sci. Technol.* **2014**, *25*, 012002.
- (3) Bharadwaj, S. R.; Varma, S.; Wani, B. N. *Functional Materials* **2012**, 639–674.
- (4) Eldada, L. J. *Nanophoton* **2011**, *5*, 051704.
- (5) Koumoto, K.; Funahashi, R.; Guilmeau, E.; Miyazaki, Y.; Weidenkaff, A.; Wang, Y.; Wan, C. J. *Am. Cera. Soc.* **2013**, *96*, 1.
- (6) Thangadurai, V.; Narayanan, S.; Pinzaru, D. *Chem. Soc. Rev.* **2014**, *43*, 4714.
- (7) Zhang, Q.; Uchaker, E.; Cao, G. *Material Matters* **2014**, *4*, 122.
- (8) Koka, A.; Zhou, Z.; Tang, H.; Soadno, H. A. *Nanotechnology* **2014**, *25*, 375603.

ENERGY HARVESTING

USING LEAD ZIRCONIUM TITANATE-BASED CERAMIC NANOWIRES



Zhi Zhou¹, Dr. Haixiong Tang¹, Dr. Henry A. Sodano^{1,2*}

¹Department of Materials Science and Engineering

²Department of Mechanical and Aerospace Engineering

University of Florida, Gainesville, Florida 32611 USA

Email: hsodano@ufl.edu

Introduction

Among various ceramics, one-dimensional (1-D) piezoelectric ceramics have attracted significant scientific attention for use in energy harvesting.¹⁻³ One-dimensional piezoelectric nanostructures are the smallest dimensional structures capable of the efficient transport of electrons and, thus, have the potential to yield high energy conversion efficiency.⁴ Further, the high mechanical strength and flexibility of the 1-D nanostructures enable sensitivity to small, random mechanical disturbances that can be converted into electrical signals useful for both energy harvesting and nanoscale sensing.⁵⁻⁷ The sensitivity of 1-D piezoelectric nanostructures is highly dependent on the properties of the piezoelectric material. This makes the identification of materials with a high piezoelectric coupling coefficient important. One-dimensional piezoelectric nanostructures, such as nanowires (NWs) comprised of ZnO, BaTiO₃, and NaNbO₃ have been studied to achieve this goal.^{6,8-11} However, the relatively low piezoelectric coupling coefficient of these compositions restricts their applications. The highest measured piezoelectric coupling coefficient for ZnO nanowires is reported to be ~13 pm/V;^{8,9} for BaTiO₃ nanowires, it is 50 pm/V.^{10,11}

Lead zirconium titanate (PZT) is considered a promising piezoelectric material for sensor and transducer applications because it exhibits outstanding piezoelectric coupling at compositions near the morphotropic phase boundary (MPB) between the tetragonal and rhombohedral phases. It has been reported that the piezoelectricity of PZT can further be enhanced by doping and thermal processing.¹²⁻¹⁴ In particular, PZT NWs have attracted scientific interest due to their potential for providing excellent piezoelectric properties in a 1-D structure.

Numerous methods have been developed to produce PZT NWs, including hydrothermal,¹⁵⁻¹⁹ template-infiltration,²⁰⁻²² electrophoresis,²³ pulsed laser deposition (PLD),²⁴ and electro-spinning.^{12,25} However, most of these methods suffer from low yield and cost concerns. In contrast, recent reports demonstrate that a two-step hydrothermal process can be used to achieve high efficiency 1-D PZT NWs with controllable composition, variable crystal size, and high yields.³

In this article, we report on our research into the structural and piezoelectric properties of hydrothermally synthesized perovskite PZT [Pb(Zr_xTi_{1-x})O₃] nanowires using the two-step approach with the Zr:Ti molar ratios of 0.52:0.48 and 0.2:0.8. The Zr:Ti molar ratios of 0.52:0.48 and 0.2:0.8 were deliberately chosen to emphasize the importance of MPB proximity on piezoelectric properties of Pb(Zr_xTi_{1-x})O₃. The ratio of 0.52:0.48 leads to PZT with composition near MPB, whereas the ratio of 0.2:0.8 keeps the Pb(Zr_xTi_{1-x})O₃ away from MPB. A refined piezoelectric force microscopy (PFM) testing method was applied to measure the coupling coefficient of the NWs. In addition, the PZT NWs were used in the fabrication and testing of an ambient mechanical vibrational energy harvester. The high piezoelectric coupling coefficient and high power density of the PZT NWs near the MPB demonstrates the potential to replace existing materials in sensing and energy harvesting applications.

Synthesis and Structural Properties

The synthesis of PZT [Pb(Zr_xTi_{1-x})O₃] NWs using a two-step hydrothermal process is summarized schematically in **Figure 1A** (experimental details regarding this can be found in reference 3). In the first step, H₂Zr_xTi_{1-x}O₃ NWs are synthesized hydrothermally using zirconium propoxide (70% in 1-propanol) (**Aldrich Prod. No. 333972**) and titanium isopropoxide as precursors (**Aldrich Prod. No. 377996**). In the second step, the H₂Zr_xTi_{1-x}O₃ NWs serve as a template and are dispersed in a Pb(NO₃)₂ solution under hydrothermal conditions to yield PZT NWs. The as-synthesized NWs crystallize in PbTiO₃-type phase (designated as the PX phase). However, they adopt the perovskite phase after heat treatment at 600 °C for 30 min. The comparison of the scanning electron micrographs (SEM) of the H₂Zr_xTi_{1-x}O₃ nanowires obtained from the first step (**Figures 1B** and **1C**), and those of the heat-treated Pb(Zr_xTi_{1-x})O₃ nanowires (**Figures 1D** and **1E**), reveal that the 1-D shape of the NWs remains unaltered when the PX phase PZT nanowires adopt the perovskite phase. The XRD pattern of Pb(Zr_xTi_{1-x})O₃ nanowires is shown in **Figure 1F**. The diffraction peaks of the XRD pattern are clearly distinguishable and can be indexed to the perovskite PZT structure, which also confirms the complete conversion from H₂Zr_xTi_{1-x}O₂ to PZT nanowires in the second synthesis step. The successful conversion is further confirmed by the presence of Pb, Zr, and Ti peaks in energy dispersive X-ray spectroscopy (EDX) patterns (**Figures 1G** and **1H**) of the PZT nanowires. The intensity of the Zr peak in the EDX pattern of Pb(Zr_{0.52}Ti_{0.48})O₃ nanowires is larger than that of Pb(Zr_{0.2}Ti_{0.8})O₃ NWs, which proves the higher Zr molar ratio in Pb(Zr_{0.52}Ti_{0.48})O₃ nanowires.

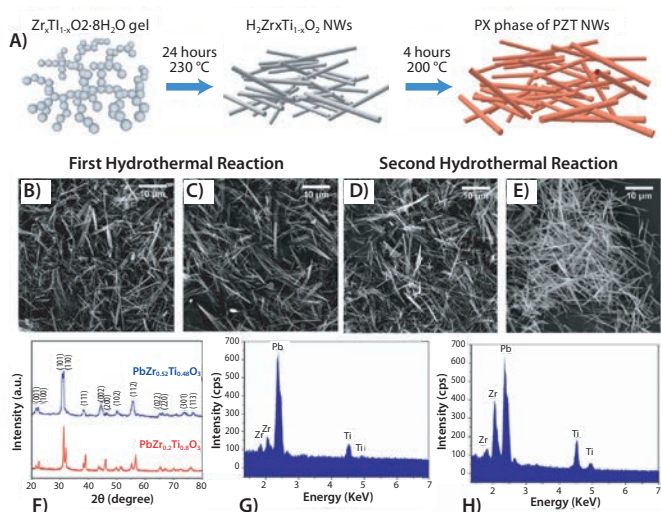


Figure 1. (A) Schematic of synthesis of PZT [Pb(Zr_xTi_{1-x})O₃] NWs using two step hydrothermal process; SEM images of (B) H₂Zr_{0.2}Ti_{0.8}O₃, (C) H₂Zr_{0.52}Ti_{0.48}O₃, (D) Pb(Zr_{0.2}Ti_{0.8})O₃, (E) Pb(Zr_{0.52}Ti_{0.48})O₃ NWs (F) XRD patterns of PZT NWs obtained after second hydrothermal step and heat treatment at 600 °C; EDX patterns of PZT [Pb(Zr_xTi_{1-x})O₃] NWs with (G) Zr:Ti=0.2:0.8 and (H) Zr:Ti=0.52:0.48.³

Piezoelectric Properties

Piezoelectric force microscopy (PFM) is a widely used technique to determine the piezoelectric properties and the application potential of piezoelectric nanowires. However, the accurate determination of the piezoelectric coupling coefficient using the PFM method severely suffers from a low signal-to-noise ratio.^{15,26} For example, measurement of the butterfly loop and phase change of PZT NWs as a function of the applied electric field by Wang et al. could not determine the piezoelectric coupling coefficient due to the poor signal-to-noise ratio.¹⁵ Xu et al. have reported that the electromechanical coupling of piezoelectric NWs can be quantitatively measured by using a built-in lock-in amplifier and a commercial PFM software package.²⁶ However, the accuracy of the electromechanical coupling obtained from the use of commercial code is considered unreliable as it only provides a single number without allowing the direct analysis of the piezoelectric response. In order to measure the piezoelectric strain coupling coefficient of the PZT NWs quantitatively, refined PFM testing was performed using the experimental setup shown schematically in **Figure 2A**.¹⁵ The samples for the PFM were prepared by drop-casting the sonicated ethanol suspension of Pb(Zr_xTi_{1-x})O₃ NWs on a Pt/Ti-coated silicon wafer and drying in air. The accurate topography of the NWs (**Figures 2B** and **2C**) was determined by performing a low scan speed (0.5 μm/s) atomic force microscopy (AFM) scan in non-contact mode. For measuring the electromechanical response, the conductive AFM tip was placed on the top facet of NWs with a force of 1,500 nN and switched to contact mode; then, triangular 1 Hz AC voltage of varying amplitudes was applied to the Pt/Ti layer on the silicon wafer. During the measurement, the AFM tip serves as the ground. The electromechanical displacement and phase response caused by the piezoelectric effect were collected 100 times; to minimize the errors associated with noise, these signals were filtered with a band pass filter centered at the waveform excitation frequency and averaged. The bipolar voltage dependence of the averaged displacement with a standard deviation of less than 30 pm from the unpoled PbZr_{0.2}Ti_{0.8}O₃ and PbZr_{0.52}Ti_{0.48}O₃ NWs are shown in **Figures 2D** and **2G**, respectively. The butterfly-like appearance of the displacement loops is attributed to the nature of domain motion and the piezoelectric properties of the PZT nanowires. The hysteresis loop of phase versus voltage from the PbZr_{0.2}Ti_{0.8}O₃ and PbZr_{0.52}Ti_{0.48}O₃ NWs, with a standard deviation of less

than 3 degrees, is shown in **Figures 2E** and **2H**, respectively. Here, the phase change from 90° to -90° during the application of the excitation waveforms originates from switching the polarization direction of the nanowire with the coercive field matching in both the phase and amplitude loops. From **Figure 2H**, the coercive field of PbZr_{0.52}Ti_{0.48}O₃ NWs of 200 nm diameter is estimated to be 50 kV/mm. The coercive field of PbZr_{0.2}Ti_{0.8}O₃ NWs is larger than the bulk materials (2.5 kV/mm) and the increase is believed to originate from the small grain size of the nanowires and from grains that are not oriented along the electric field direction.²⁷⁻²⁹ The piezoelectric coupling coefficient (*d*₃₃) of the PZT PbZr_{0.2}Ti_{0.8}O₃ (40 ± 5 pm/V) and PbZr_{0.52}Ti_{0.48}O₃ (80 ± 5 pm/V) NWs was determined from the displacement versus unipolar voltage loops shown in **Figures 2F** and **2I**, respectively. We note that the *d*₃₃ for PbZr_{0.52}Ti_{0.48}O₃ is larger than that of PbZr_{0.2}Ti_{0.8}O₃. This indicates that the enhanced electromechanical coupling of PbZr_{0.52}Ti_{0.48}O₃ can be attributed to its proximity to the morphotropic phase boundary between the ferroelectric rhombohedral and tetragonal phases brought about by the higher concentration of Zr. The *d*₃₃ value of PbZr_{0.52}Ti_{0.48}O₃ NWs (80 pm/V) was found to be larger than that of prototype PZT NWs (50 pm/V) and ZnO nanowires (13 pm/V), which are widely used in energy harvesters.^{8,9,15}

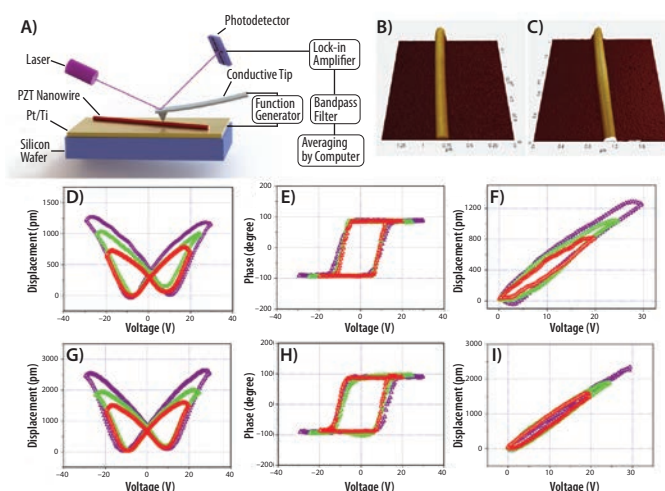


Figure 2. (A) Schematics of piezoelectric force microscopy (PFM) testing setup; (B) topography of PbZr_{0.2}Ti_{0.8}O₃ and (C) PbZr_{0.52}Ti_{0.48}O₃ NWs. Displacement of PZT nanowires when subjected to three bipolar excitation waveforms of varying amplitude for (D) PbZr_{0.2}Ti_{0.8}O₃ and (G) PbZr_{0.52}Ti_{0.48}O₃. Phase change of PZT nanowires when subjected to three bipolar excitation waveforms of varying amplitude: (E) PbZr_{0.2}Ti_{0.8}O₃ and (H) PbZr_{0.52}Ti_{0.48}O₃. Displacement of PZT nanowires when subjected to three unipolar excitation waveforms of varying amplitude: (F) PbZr_{0.2}Ti_{0.8}O₃ and (I) PbZr_{0.52}Ti_{0.48}O₃.³

Energy Harvesting

The energy harvesting performance of the new PZT NWs was further demonstrated by fabricating a nanocomposite by combining PZT NWs with polydimethylsiloxane (PDMS). The PDMS is chosen as a matrix because it not only protects the NWs from the strain generated in the energy harvesting test, but due to its large elasticity and ability to hold over 100% of tensile strain without mechanical failure, it can also withstand large deformation.^{30,31} The mixture of PZT NWs and PDMS is first tape-casted on a Ti foil coated with Au (Ti thickness = 35 μm; Au coating = 20 nm) and then cured at 150 °C for 12 hr. The Ti foil serves as the bottom electrode in the device. To ensure the alignment of the PZT NWs dipoles in the direction of the electric field, which is normal to the face bottom Ti electrode, the cured mixture was poled at 150 °C for 2 hr with a custom corona poling setup at 15 kV. After this, a 200 nm thick silver leaf, which acts as the second electrode, is overlaid on the top of the nanocomposite.

Figures 3A and 3B show the schematic of the energy harvester and the cross-sectional view of the 50:50 wt % nanocomposite of $\text{PbZr}_{0.52}\text{Ti}_{0.48}\text{O}_3$ NWs and PDMS, respectively. In the energy harvester, under stress induced by vibration, the PZT nanowires generate potential differences between the two electrodes and serve as an energy generation source. Figure 3B shows that the NWs are well distributed throughout the PDMS matrix. For the nanocomposite, the maximum weight percent of NWs was set to 50%, as higher concentrations might lead to poor dispersion of the NWs. In the energy harvester, the nanocomposite serves as a cantilever which can easily vibrate at the resonant frequency. The cantilever is formed by attaching the root of the nanocomposite beam to a glass substrate with epoxy (Figure 3A). In order to perform a power density comparison for all energy harvesters tested here, the dimensions of the nanocomposite was kept at ~ 2 cm (L) \times 1 cm (W) \times 0.018 cm (T).

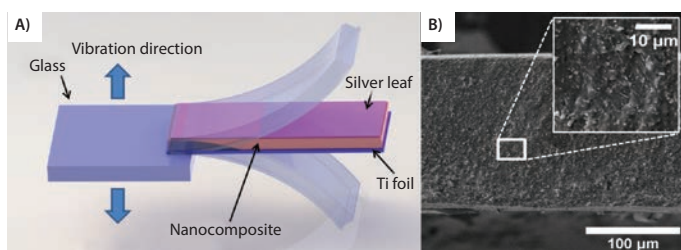


Figure 3. (A) Schematics of PZT/PDMS nanocomposite-based energy harvester. (B) A cross-section image of the 50:50 wt % $\text{PbZr}_{0.52}\text{Ti}_{0.48}\text{O}_3$ NWs and PDMS nanocomposite.³

To investigate the application potential of the PZT NWs and PDMS nanocomposite, the voltage and current generated from the nanocomposite was first screened by periodic manual bending and releasing. The periodic manual bending and releasing is the commonly adopted method used for primary screening of the application potential of nanocomposite-based energy harvesters. The open circuit voltage (V_{oc}) was measured by a high impedance (1 T Ω) voltmeter, and the short circuit current (I_{sc}) was measured by a high speed electrometer. The V_{oc} graph of the 50:50 wt % $\text{PbZr}_{0.52}\text{Ti}_{0.48}\text{O}_3$ NWs PDMS nanocomposite-based energy harvester is shown in Figure 4A. Under periodic bending and release, the device generates voltages ranging between 6 to 7 V, which is more than twice that of a NaNbO_3 NWs nanocomposite (3.2 V) and 3 times larger than a ZnO NWs nanocomposite (2.03 V).^{32,33} The large peak value of V_{oc} in present nanocomposites can be attributed to the enhanced piezoelectric coefficient of $\text{PbZr}_{0.52}\text{Ti}_{0.48}\text{O}_3$ NWs. However, it should be emphasized that merely a comparison of peak V_{oc} does not fully demonstrate the advancement of PZT/PDMS nanocomposites since it also highly depends on strain rate. Therefore, a controlled excitation is a must to quantify the actual performance. Figure 4C shows the magnified V_{oc} graph. Associated with bending strain, the V_{oc} shows a negative peak, which is followed by a large positive peak corresponding to the release of the bent nanocomposite, resulting in a large strain rate. The I_{sc} output graph from the energy harvester device is shown in Figure 4B. The periodic bending and release continuously generates a current ranging between 100 to 120 nA. The oscillation of the V_{oc} and I_{sc} observed in Figures 4C and 4D, respectively, is attributed to the damping effect of the cantilever, and it further confirms that the output signals were, indeed, generated by the PZT/PDMS nanocomposite.

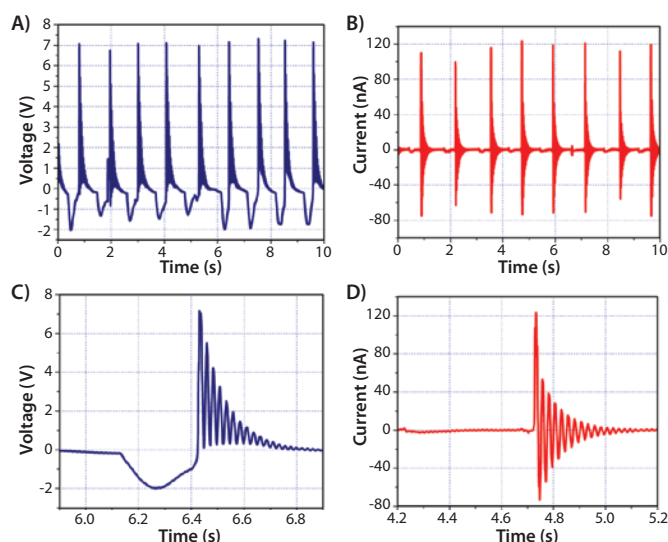


Figure 4. Signal generation from the 50:50 wt % $\text{PbZr}_{0.52}\text{Ti}_{0.48}\text{O}_3$ NWs and PDMS nanocomposite-based energy harvester. (A) Open circuit voltage and (B) short circuit current generation from periodic, manual bending and releasing of the cantilevered sample with magnified views of the (C) voltage output and (D) current output.³

Typically, ambient vibrational energy exists in the 1 Hz to 1 kHz range.^{34,35} Thus, the performance of the PZT/PDMS nanocomposite energy harvester for ambient mechanical vibrations, and a dynamic characterization using frequency response function (FRF) was performed.³ For the nanocomposite cantilever, the FRF reveals a resonant frequency of 43 Hz.

In order to demonstrate the potential for high-performance nanocomposite energy harvesting with PZT nanowires at relatively low frequencies, the alternating current (AC) power and power density were calculated with respect to varying load resistors. The AC power (P_L) was determined by measuring the root mean square (RMS) voltage (V_L) across external resistive load (R_L , ranging from 1 M Ω to 500 M Ω) at the resonant frequency using Equation 1:³⁶

$$P_L = I_{L(RMS)}^2 R_L = \left\{ \frac{V(RMS)}{Z_S + R_L} \right\}^2 R_L = \frac{V_L^2(RMS)}{R_L} \quad (1)$$

Figures 5A and 5B show the AC power and power density, respectively, from the 50:50 wt % $\text{PbZr}_{0.52}\text{Ti}_{0.48}\text{O}_3$ NWs PDMS energy harvester. For an R_L below 30 M Ω , the power increases rapidly and peaks at a value of 88 nW for $R_L = 40$ M Ω .^{34,37} For $R_L > 40$ M Ω , the power continues to reduce since V_L starts saturating toward the V_{oc} . Figures 5C and 5D show concentration dependence of V_{pp} and power density of PZT NWs/PDMS nanocomposites. For both $\text{PbZr}_{0.52}\text{Ti}_{0.48}\text{O}_3$ and $\text{PbZr}_{0.2}\text{Ti}_{0.8}\text{O}_3$ nanocomposites, the V_{pp} and power density increase with increasing concentration. The maximum power density for 50:50 wt % PZT NWs and PDMS harvesters with $\text{PbZr}_{0.52}\text{Ti}_{0.48}\text{O}_3$ and $\text{PbZr}_{0.2}\text{Ti}_{0.8}\text{O}_3$ was estimated to be 2.4 and 0.75 $\mu\text{W}/\text{cm}^3$, respectively (Figure 5D). The higher power density value (~ 3 times) for the $\text{PbZr}_{0.52}\text{Ti}_{0.48}\text{O}_3$ -based nanocomposite compared to $\text{PbZr}_{0.2}\text{Ti}_{0.8}\text{O}_3$ is attributed to the enhanced piezoelectric properties of $\text{PbZr}_{0.52}\text{Ti}_{0.48}\text{O}_3$ brought about by the proximity of the material to MPB.

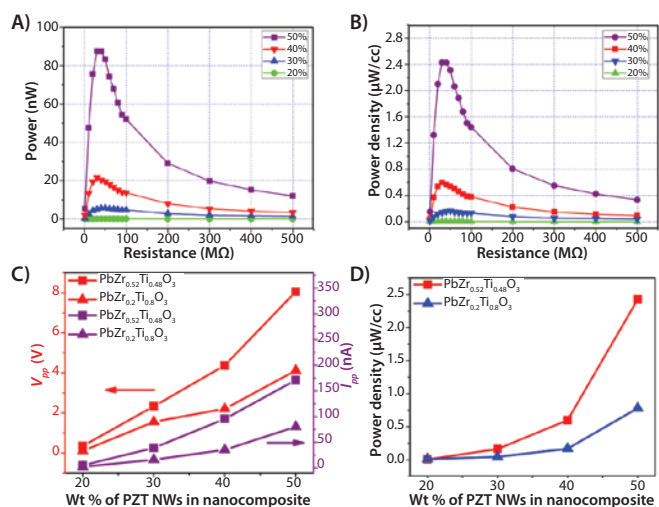


Figure 5. Power characterization of PZT/PDMS nanocomposite-based energy harvesters. (A) AC power and (B) power density of the $\text{PbZr}_{0.52}\text{Ti}_{0.48}\text{O}_3$ /PDMS nanocomposite energy harvester with varying load resistors (R_L) showing a peak power of 88 nW and a peak power density of $2.4 \mu\text{W}/\text{cm}^3$ at an optimal R_L of 40 MΩ. This peak power level increases with increasing weight percent of $\text{PbZr}_{0.52}\text{Ti}_{0.48}\text{O}_3$ nanowires. (C) V_{pp} , I_{pp} , and (D) peak power density of PZT/PDMS nanocomposite energy harvester is increased by increasing PZT nanowires weight percent.³

Conclusions

The importance of the morphotropic phase boundary (MPB) on the piezoelectric properties has been demonstrated. A high power density ($2.4 \mu\text{W}/\text{cm}^3$) for the $\text{PbZr}_{0.52}\text{Ti}_{0.48}\text{O}_3$ NWs/PDMS nanocomposite-based energy harvester was obtained at a relatively low frequency. This power density is comparable to several cantilever-based energy harvesters stimulated by base vibration^{38–40} and demonstrates the application potential of PZT NWs in energy harvesting and sensing. Furthermore, by using the two-step hydrothermal process, these PZT NWs with tunable composition can be synthesized at high yield, increasing their importance in energy harvesting and sensing applications.

Acknowledgment

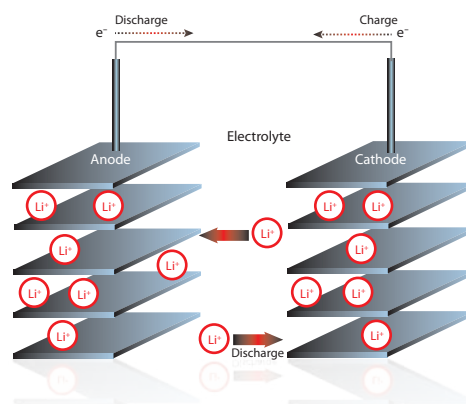
The authors gratefully acknowledge support from the Air Force Office of Scientific Research under contract FA9550-12-1-0132.

PRODUCT HIGHLIGHT

Make Your Own Lithium-ion Batteries

Applications of lithium-ion batteries (LIBs) extend from modern electronics to automobiles. Order *ready-to-use* electrolyte solutions and electrode sheets in *battery grade* to fabricate your LIB.

For a complete list of LIB materials, including electrode powders, electrolytes, solvents and additives, visit aldrich.com/lib



References

- Qiu, Y.; Yang, D. C.; Yin, B.; Lei, J. X.; Zhang, H. Q.; Zhang, Z.; Chen, H.; Li, Y. P.; Bian, J. M.; Liu, Y. H.; Zhao, Y.; Hu, L. Z. *RSC Adv.* **2014**, *5*, 5941.
- Yuan, D.; Yang, Y.; Hu, Q.; Wang, Y. *J. Am. Ceram. Soc.* **2014**, *97*, 3999.
- Zhou, Z.; Tang, H.; Sodano, H. A. *Adv. Mater.* **2014**, *26*, 7547.
- Rørvik, P. M.; Grande, T.; Einarsrud, M. *Adv. Mater.* **2011**, *23*, 4007.
- Hochbaum, A. I.; Yang, P. *Chem. Rev.* **2010**, *110*, 527.
- Jung, J. H.; Lee, M.; Hong, J.; Ding, Y.; Chen, C.; Chou, L.; Wang, Z. L. *ACS Nano.* **2011**, *5*, 10041.
- Xu, S.; Yeh, Y.; Poirier, G.; McAlpine, M. C.; Register, R. A.; Yao, N. *Nano Lett.* **2013**, *13*, 2393.
- Wang, Z. L. *J. Phys.: Condens. Matter.* **2004**, *16*, 829.
- Fan, H. J.; Lee, W.; Hauschild, R.; Alexe, M.; Le Rhun, G.; Scholz, R.; Dadgar, A.; Nielsch, K.; Kalt, H.; Krost, A. *Small.* **2006**, *2*, 561.
- Tang, H.; Lin, Y.; Sodano, H. A. *Adv. Energy Mater.* **2013**, *3*, 451.
- Urban, J. J.; Yun, W. S.; Gu, Q.; Park, H. J. *Am. Chem. Soc.* **2002**, *124*, 1186.
- Chen, X.; Xu, S.; Yao, N.; Shi, Y. *Nano Lett.* **2010**, *10*, 2133.
- Chen, Y.; Liu, T.; Chen, C.; Liu, C.; Chen, S.; Wu, W.; Wang, Z. L.; He, J.; Chu, Y.; Chueh, Y. *ACS Nano.* **2012**, *6*, 2826.
- Isarakorn, D.; Briand, D.; Janphuang, P.; Sambri, A.; Gariglio, S.; Triscone, J. M.; Guy, F.; Reiner, J. W.; Ahn, C. H.; Rooij, N. F. *Smart Mater. Struct.* **2011**, *20*, 025015.
- Wang, J.; Sandu, C.; Setter, N. *IEEE Trans. Ultrason. Ferroelectr. Freq. Control.* **2009**, *56*, 1813.
- Wang, J.; Sandu, C.; Colla, E.; Wang, Y.; Ma, W.; Gysel, R.; Trodahl, H.; Setter, N.; Kuball, M. *Appl. Phys. Lett.* **2007**, *90*, 133107.
- G. Xu, Z. Ren, P. Du, W. Weng, G. Shen, G. Han, *Adv. Mater.* **2005**, *17*, 907.
- H. Tang, Y. Lin, H. A. Sodano, *Adv. Energy Mater.* **2012**, *2*, 393.
- H. Tang, Y. Lin, C. Andrews, H. A. Sodano, *Nanotechnology.* **2011**, *22*, 015702.
- A. Bernal, A. Tselev, S. Kalinin, N. Bassiri-Gharb, *Adv. Mater.* **2012**, *24*, 1160.
- X. Zhang, X. Zhao, C. Lai, J. Wang, X. Tang, J. Dai, *Appl. Phys. Lett.* **2004**, *85*, 4190.
- S. J. Limmer, S. Seraji, Y. Wu, T. P. Chou, C. Nguyen, G. Z. Cao, *Adv. Funct. Mater.* **2002**, *12*, 59.
- S. J. Limmer, S. Seraji, M. J. Forbess, Y. Wu, T. P. Chou, C. Nguyen, G. Z. Cao, *Adv. Mater.* **2001**, *13*, 1269.
- Y. Z. Chen, T. H. Liu, C. Y. Chen, C. H. Liu, S. Y. Chen, W. W. Wu, Z. L. Wang, J. H. He, Y. H. Chu, Y. L. Chueh, *ACS Nano.* **2012**, *6*, 2826.
- J. Feenstra, H. A. Sodano, *J. Appl. Phys.* **2008**, *103*, 124108.
- S. Xu, G. Poirier, N. Yao, *Nano Lett.* **2012**, *12*, 2238.
- C. A. Randall, N. Kim, J. Kucera, W. Cao, T. R. Shrout, *J. Am. Ceram. Soc.* **1998**, *81*, 677.
- A. Gruverman, S. V. Kalinin, *J. Mater. Sci.* **2006**, *41*, 107.
- J. Liu, S. Zhang, H. Zeng, C. Yang, Y. Yuan, *Phys. Rev. B.* **2005**, *72*, 172101.
- Y. Qi, J. Kim, T. D. Nguyen, B. Lisko, P. K. Purohit, M. C. McAlpine, *Nano Lett.* **2011**, *11*, 1331.
- G. Y. Yang, V. J. Bailey, Y. Wen, G. Lin, W. C. Tang, J. H. Keyak, *Sensors, 2004. Proceedings of IEEE.* **2004**, *3*, 1355.
- J. H. Jung, M. Lee, J. Hong, Y. Ding, C. Chen, L. Chou, Z. L. Wang, *ACS Nano.* **2011**, *5*, 10041.
- G. Zhu, R. Yang, S. Wang, Z. L. Wang, *Nano Lett.* **2010**, *10*, 3151.
- A. Koka, H. A. Sodano, *Adv. Energy Mater.* **2014**, *1301660*.
- A. Koka, Z. Zhou, H. A. Sodano, *Energy Environ. Sci.* **2014**, *7*, 288.
- S. Priya, *J. Electroceram.* **2007**, *19*, 167.
- Y. Liao, H. A. Sodano, *Smart Mater. Struct.* **2008**, *17*, 065026.
- V. R. Challa, M. Prasad, F. T. Fisher, *Smart Mater. Struct.* **2009**, *18*, 095029.
- L. Gu, C. Livermore, *Smart Mater. Struct.* **2011**, *20*, 045004.
- S. Roundy, P. K. Wright, J. Rabaey, *Comput. Commun.* **2003**, *26*, 1131.

Piezoelectric Materials

For a complete list of available materials, visit aldrich.com/periodic.

Name	Purity (%)	Particle Size	Form	Prod. No.
Barium strontium titanium oxide	>99	<100 nm (APS)	nanopowder	633828-25G 633828-100G
	99.995	-	powder	256552-10G
Barium titanate(IV)	99.5	<2 μm	powder	338842-100G 338842-500G
	99.9	50 nm (SEM)	nanopowder (cubic)	745952-100G
	-	<10 μm	powder	383309-250G
Lanthanum calcium borate	99.9	-200 mesh	powder	772666-25G
Lead magnesium niobate	≥ 99	-	powder	672874-25G
Lead(II) titanate	≥ 99	<5 μm	powder	215805-250G
Lead(II) zirconate	99	-325 mesh	powder	398888-50G
Potassium niobate	-	-	powder	541206-25G
Zinc niobate	97	-	powder	548588-50G

Nanostructures and Nanomaterials for Energy Applications

Nanowires

For a complete list of available materials, visit aldrich.com/nanomaterial.

Name	Dimensions (nm)	Description	Prod. No.
Aluminum oxide	2-6 \times 200-400	nanowires	551643-10G 551643-50G
Gold nanowires	30 \times 4,500	$\geq 50 \mu\text{g/mL}$ dispersion (H_2O)	716944-10ML
	30 \times 6,000	$> 50 \mu\text{g/mL}$ dispersion (H_2O)	716952-10ML
Nickel(III) oxide	$\sim 20 \text{ nm} \times \sim 10 \mu\text{m}$	nanowires	774545-500MG
Silver nanowires	115 nm \times 20-50 μm	0.5% (isopropyl alcohol suspension) liquid (suspension)	739448-25ML
	60 nm \times 10 μm	0.5% (isopropyl alcohol suspension) liquid (suspension)	739421-25ML
	120-150 nm \times 20-50 μm	0.5% (isopropyl alcohol suspension) liquid (suspension)	778095-25ML
Titanium(IV) oxide	$\sim 100 \text{ nm} \times \sim 10 \mu\text{m}$	nanowires	774510-500MG
	$\sim 10 \text{ nm} \times \sim 10 \mu\text{m}$	nanowires	774529-500MG
Tungsten(VI) oxide	$\sim 50 \text{ nm} \times \sim 10 \mu\text{m}$	nanowires	774537-500MG
Zinc oxide	90 nm \times 1 μm	nanowires	773999-500MG
	50 \times 300	nanowires	773980-500MG
	300 nm \times 4-5 μm	nanowires	774006-500MG

Gold Nanorods

For a complete list of available materials, visit aldrich.com/nanomaterial.

Name	Dimension	Absorption	Concentration	Form	Prod. No.
Gold nanorods	diam. \times L 25 nm \times 34 nm ($\times \pm 10$)	550 nm	$> 45 \mu\text{g/mL}$	colloidal suspension dispersion in H_2O	771643-25ML
	diam. \times L 25 \times 47 nm ($\times \pm 10$)	600 nm	$> 45 \mu\text{g/mL}$	colloidal suspension dispersion in H_2O	771651-25ML
	diam. \times L 25 \times 60 nm ($\times \pm 10$)	650 nm	$> 45 \mu\text{g/mL}$	colloidal suspension dispersion in H_2O	771686-25ML
	diam. \times L 10 \times 38 $\pm 10\%$ nm	780 nm	$> 30 \mu\text{g/mL}$	colloidal suspension dispersion in H_2O	716812-25ML
	diam. \times L 10 \times 41 nm $\pm 10\%$	808 nm	$> 30 \mu\text{g/mL}$	colloidal suspension dispersion in H_2O	716820-25ML
	diam. \times L 10 \times 41 nm $\pm 10\%$	808 nm	$\geq 1800.0 \mu\text{g/mL}$	colloidal suspension dispersion in H_2O	716898-1ML
	diam. \times L 9.5-11.5 \times 40-50 nm	808 nm	$> 30 \mu\text{g/mL}$	dispersion in H_2O	747998-5ML

Gold Nanorods (cont'd)

Name	Dimension	Absorption	Concentration	Form	Prod. No.
Gold nanorods	diam. x L 10 x 45 nm ±10%	850 nm	> 30 µg/mL	colloidal suspension dispersion in H ₂ O	716839-25ML
	diam. x L 9-11 x 41-48 nm	850 nm	> 30 µg/mL	dispersion in H ₂ O	748005-5ML
	diam. x L 10 x 50 (x ±10)	900 nm	≥ 30 µg/mL	colloidal suspension dispersion in H ₂ O	776653-25ML
	diam. x L 10 x 59 nm (x ±10)	980 nm	> 30 µg/mL	colloidal suspension dispersion in H ₂ O	776661-25ML
	diam. x L 10 x 67 nm (x ±10)	980 nm	> 30 µg/mL	colloidal suspension dispersion in H ₂ O	776688-25ML
	diam. x L 25 x 75 nm	-	100 µg/mL	colloidal suspension dispersion in H ₂ O	716936-10ML

Nanopowders and Dispersions

For a complete list of available materials, visit aldrich.com/nanopowders.

Name	Size	Description	Form	Prod. No.
Aluminum oxide	particle size 30 - 60 nm (TEM)	-	liquid (suspension) nanoparticles	642991-100ML
	particle size <50 nm (DLS)	-	nanoparticles	702129-100G 702129-500G
	particle size <50 nm (TEM)	gamma phase	nanopowder	544833-10G 544833-50G
	primary particle size 13 nm (TEM)	99.8% trace metals basis	nanopowder	718475-100G
Titanium	particle size <100 nm	98.5% trace metals basis	dispersion nanoparticles	513415-5G
Titanium carbide	particle size <200 nm (TEM)	-	nanopowder	636967-25G 636967-250G
Titanium(IV) oxide	particle size <100 nm (BET)	≥97%	nanopowder	677469-5G
	primary particle size 21 nm (TEM)	≥99.5% trace metals basis	nanopowder	718467-100G
Titanium(IV) oxide, anatase	particle size <25 nm	99.7% trace metals basis	nanopowder	637254-50G 637254-100G 637254-500G
Titanium(IV) oxide, brookite	<100 nm	99.99% trace metals basis	nanopowder	791326-5G
Titanium(IV) oxide, mixture of rutile and anatase	particle size <50 nm (XRD)	99.5% trace metals basis	nanopowder	634662-25G 634662-100G
	particle size <100 nm (BET)			
	particle size ~21 nm (primary particle size of starting nanopowder)	99.9% trace metals basis	nanoparticles paste	700355-25G
	particle size <250 nm (DLS)			
Titanium(IV) oxide, rutile	particle size <150 nm (volume distribution, DLS)	99.5% trace metals basis	dispersion nanoparticles	700347-25G 700347-100G
	particle size ~21 nm (primary particle size of starting nanopowder)			
Titanium(IV) oxide, rutile	particle size <100 nm, diam. x L ~10 x ~40 nm	99.5% trace metals basis	nanopowder	637262-25G 637262-100G 637262-500G
Titanium silicon oxide	particle size <50 nm (BET)	99.8% trace metals basis	nanopowder	641731-10G 641731-50G
Zinc	particle size <50 nm	≥99% trace metals basis	nanopowder	578002-5G
Zinc oxide	particle size <100 nm	~80% Zn basis	nanopowder	544906-10G 544906-50G
	particle size <50 nm (BET)	>97%	nanopowder	677450-5G
Zinc oxide, dispersion	avg. part. size <35 nm (APS)	-	nanoparticles	721077-100G
	particle size <100 nm (DLS)			
	avg. part. size <35 nm (APS)	-	nanoparticles	721093-100G
	particle size <110 nm (DLS)			
Zinc oxide, dispersion	avg. part. size <35 nm (APS)	-	nanoparticles	721107-100G
	particle size <120 nm (DLS)			

INTRODUCTION TO INORGANIC NANOMATERIALS



Meenakshi Hardi, Market Segment Manager
Aldrich Materials Science

In the past decade, nanotechnology has experienced rapid growth due to both significant advances in nanofabrication techniques and to the large variety of applications of nanostructured materials in the areas of biomedical, electronics, and energy.¹⁻⁴ The seminal idea of nanotechnology was first proposed in 1959 by Nobel award winner Richard Feynman in his speech entitled "There's Plenty of Room at the Bottom." In this speech, Feynman discussed the importance "of manipulating and controlling things on a small scale" and described how physical properties of nanomaterials differ significantly from those of conventional materials due to large surface-to-volume ratios as well as quantum effects. Nanomaterials come in many varieties, including nanoparticles, nanoclusters, nanocrystals, nanotubes, nanofibers, nanowires, nanorods, nanofilms, and others. They can be carbon based or made of inorganics (such as metals, semiconductors, oxides), as well as many other materials. **Figure 1** shows the TEM image of typical gold nanorods as a representative example.

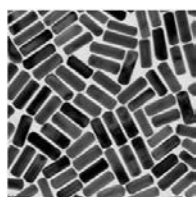


Figure 1. TEM image of typical gold nanorods (10 nm × 40 nm). Gold nanorods are used for *in vivo* imaging.

Inorganic nanomaterials have unique size- and shape-dependent optical, chemical, electrical, magnetic, mechanical, and other properties that make them suitable for a variety of applications. Examples include fuel cells; high-energy density batteries; photovoltaics and other energy generation and storage devices; nanofabricated semiconductors; and nanoscale magnetic materials used in electronic and data storage devices; as well as nanocomposite materials, catalysts, and nanostructured membranes for high-sensitivity sensors, water purification, and chemical and biomedical applications.⁴⁻¹¹

Of the many applications of nanomaterials, biomedical applications have gathered an increasing share of the research focus in recent years because they can offer new approaches for the understanding, diagnosis, and treatment of disease.⁹ Because nanomaterials are often the same size as many proteins and cellular components, they can enter and interact with living cells and their constituents in unique ways.¹⁰ Nanoparticles can be functionalized with biologically active agents such as drugs to offer a more targeted and controlled drug delivery mechanism. The nanoparticle surface can be functionalized to bind to cancerous or other types of cells. Gold nanoparticles can be engineered to undergo a property change (such as color) upon release of a drug at the target.^{11,12} Once visible to medical imaging techniques, nanomaterials can be used as markers to monitor the treatment of disease, for example, the gold nanorods shown in **Figure 1** can be used for *in vivo* imaging applications. Similarly, nanomaterials can be designed to recognize certain molecular species and for use as bio sensors.

In this anniversary issue we have invited Prof. D. Bahadur to write a mini-review on applications of magnetic nanoparticles for cancer theranostics. The following article presents an overview of the therapeutic performance of surface functionalized iron oxide-based ferrofluids (suspension of magnetic nanoparticles) toward various cancer cell lines. The surface functionalization induces multifunctionality in these ferrofluids making them thermo- and/or pH-responsive and have been successfully tested for the delivery of both hydrophilic and hydrophobic drugs.

References

- (1) Fendler, J. H. *Chem. Mater.* **1996**, *8*(8), 1616.
- (2) Pileni, M-P. *Nature Mater.* **2003**, *2*(3), 145.
- (3) Sun, Y.; Gao, S.; Lei, F.; Xiao, C.; Xie, Y. *Acc. Chem. Res.* **2015**, *48*(1), 3.
- (4) Nanomaterials, *Material Matters*, **2009**, 4(1).
- (5) Katz, H. E. *Chem. Mater.* **2004**, *16*(23), 4748.
- (6) Dai, Y.; Wang, Y.; Liu, B.; Yang, Y. *Small* **2015**, *11*(3), 268.
- (7) Zhang, Q.; Wang, C-F.; Ling, L-T.; Chen, S. J. *Mater. Chem. C: Materials for Optical and Electronic Devices* **2014**, *2*(22), 4358.
- (8) Nanomaterials for Advanced Applications, *ChemFiles*, **2005**, 5(3).
- (9) Liang, R.; Wei, M.; Evans, D. G.; Duan, X. *Chem. Commun.* **2014**, *50*(91), 14071.
- (10) Treuel, L.; Jiang, X.; Nienhaus, G.U. *J. R. Soc. Interface*, **2013**, *10*(82), 20120939.
- (11) Daniel, M-C.; Astruc, D. *Chem. Rev.* **2004**, *104*(1), 293.
- (12) Sisay, B.; Abbrha, S.; Yilma, Z.; Assen, A.; Molla, F.; Tadese, E.; Wondimu, A.; Gebre-Samuel, N.; Pattnaik, G. *J. Drug Delivery and Therapeutics* **2014**, *4*(5), 79.

MAGNETIC NANOPARTICLES FOR CANCER THERANOSTICS



Saumya Nigam,¹ Lina Pradhan,² and D. Bahadur*³

¹IITB-Monash Research Academy, IIT Bombay, Powai, Mumbai, India

²Centre for Research in Nanotechnology & Science IIT Bombay, Powai, Mumbai, India

³Department of Metallurgical Engineering and Materials Science, IIT Bombay,

Powai, Mumbai, India

Email: dhiren@iitb.ac.in

Introduction

The recent emergence of a number of highly functional nanomaterials has enabled new approaches to the understanding, diagnosis, and treatment of cancer. Of these, a variety of functional magnetic nanoparticles, including superparamagnetic ferrite nanoparticles of iron, cobalt, manganese, and nickel have proven themselves as particularly beneficial for biomedical applications.¹⁻⁶ In particular, multifunctional ferrofluids (MFs) are now being intensively studied in order to unlock their promise for future therapies.^{5,6}

A ferrofluid is a suspension of magnetic nanoparticles which behaves as a “liquid magnet” under the presence of a permanent magnetic field. Ferrofluids can be easily modified to contain different surface functional groups of both biological and non-biological origin^{7,8} for the conjugation of therapeutic payloads and imaging molecules, enabling enhanced specificity in targeted therapeutics and diagnostics. Furthermore, MFs exhibit the unique capability to produce heat when exposed to an alternating magnetic field.⁹ Since cancer cells exhibit low tolerance for elevated temperatures (above 42 °C), it is expected that localized heat from MFs could be used for the targeted treatment of cancer cells (hyperthermia treatment).¹⁰⁻¹² Magnetic hyperthermia can also be used to aid in the release of a therapeutic payload from MFs, resulting in enhanced release efficiency in the immediate tumor environment.

MFs exhibit a number of unique characteristics that have the potential to impart significant therapeutic advantages, including:

- Aqueous colloidal stability with minimal particle agglomeration
- Enhanced loading efficiencies as a platform for both hydrophilic and hydrophobic drugs
- Encapsulation of multiple drugs in a single system
- Triggered and controlled release of a drug at the target site under the influence of external stimuli like pH, temperature, AC magnetic field, and ultrasound
- Appreciable biocompatibility and biodegradability
- Rapid clearance by reticulo-endothelial system (RES) of the body

- Reduction of circulating concentration of free drug, thereby reducing side effects
- Minimization of multidrug resistance at the targeted tumor site
- Simultaneous use for MR imaging and other diagnostic applications

Recently, we have developed a variety of iron oxide-based MF hybrid systems with different surface functionalization including dendrimers,¹³ lipids,¹⁴ hydrogels,¹⁵ bio-degradable polymers, citric acid,¹⁶ and silica.¹⁷ The surface functional groups allow multifunctionality in these iron oxide-based ferrofluids and make them thermo- and/or pH-responsive.^{13,14} The iron oxide based MFs are highly stable in aqueous conditions and have been successfully tested for the delivery of both hydrophilic and hydrophobic drugs, along with magnetic hyperthermia applications in cancer cell lines as well as in subcutaneous tumor models in mice. This article presents an overview of the therapeutic performance of following systems toward various cancer cell lines:

- Stimuli-responsive magnetic nanohydrogels (MNHGs)
- T_c -tuned magnetic nanovesicles
- Dendrimer-functionalized magnetic nanoparticles
- Thermo- and pH-responsive thin lipid layer coated mesoporous magnetic nanoassemblies (LMMNA)

These formulations have also been evaluated for their performance in dual mode cancer therapy, utilizing magnetic hyperthermia in synergy with chemotherapy, non-invasive MR imaging, and electrochemical biosensing. Some of these hybrid systems have been further explored for *in vivo* applications.

Stimuli-responsive Magnetic Nanohydrogels

Hydrogels are hydrophilic, crosslinked polymers existing in a colloidal gel state. Due to their tailorable physical, chemical, and biological properties, they have been tested in numerous biomedical applications. It has been shown that the encapsulation of ferrofluids within hydrogels can result in improved biomedical properties.¹⁸ For example, Lin et al. reported the delivery of chemically modified antisense RNA oligonucleotides using degradable poly(ethylene glycol) (PEG)-based hydrogels as a promising cancer therapy.¹⁹ Zhang and co-workers successfully employed chitosan and β -glycerophosphate-based magnetic hydrogels for sustained delivery of the BCG vaccine in the treatment of bladder cancer in female Wistar rats.²⁰ Baeza and co-workers utilized the thermo-responsive copolymer of poly(ethyleneimine)-*b*-poly(*N*-isopropyl acrylamide) in combination with mesoporous silica and iron oxide nanoparticles as a platform for magnetic field induced drug release to combat multidrug resistance in cancer cells.²¹

Our group developed a poly(*N*-isopropyl acrylamide)-chitosan encapsulated Fe₃O₄ magnetic nanostructure (MNS)-based magnetic nanohydrogel (MNHG), which has been successful in combining cancer chemotherapeutics with non-invasive magnetic resonance imaging (MRI).²² The measured MRI T_2 contrast (transverse spin relaxation)

enhancement and the associated delivery efficacy of absorbed therapeutic cargo is shown **Figure 1**. Note that the hydrogel-MNS (HGMNS) system encapsulated with PEG functionalized Fe_3O_4 exhibits a higher relaxivity rate (r_2) of $173 \text{ mM}^{-1}\text{s}^{-1}$ compared to $129 \text{ mM}^{-1}\text{s}^{-1}$ obtained for a hydrogel-MNS system encapsulated with POSS functionalized Fe_3O_4 . The studies with PEG-functionalized HGMNS conjugated to doxorubicin (DOX) (**Sigma Prod. No. D1515**) have revealed a ~ 2 -fold enhancement in drug release during 1 h RF (radio-frequency) field exposure followed by 24 h incubation at 37°C . The enhanced release of therapeutic cargo in this case is attributed to microenvironmental heating in the surroundings as well as to the magneto-mechanical vibrations caused by high frequency RF inside the hydrogels. Also, RF-induced drug delivery studies with cervical cancer cell lines (HeLa) for PEG-functionalized HGMNS show more than 80% cell death. These results suggest that magnetic hydrogel system has *in vivo* theranostic potential given its high MR contrast enhancement, encapsulated MNS, and RF-induced localized therapeutic delivery.

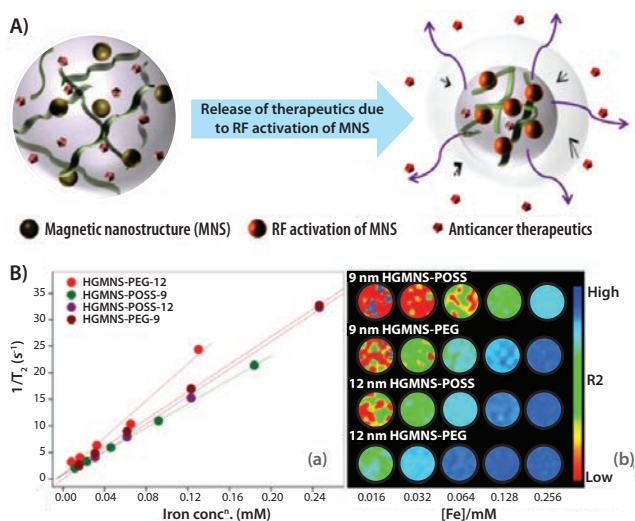


Figure 1. A) Schematic depicting the thermo-responsive collapse of the magnetic nanohydrogel due to RF exposure leading to the release of the therapeutic drug and **B)** MR contrast characteristics of magnetic nanohydrogel. The r_2 is the slope of the straight-fit line drawn for $1/T_2$ vs. iron concentrations of the corresponding sample; T_2 -weighted phantom images at five serially diluted iron concentrations of the same samples.²²

We have also explored the *in vivo* evaluation of thermo-responsive poly(*N*-isopropyl acrylamide)-chitosan based magnetic nanohydrogel (MNHG) in a subcutaneous fibrosarcoma tumor model for use in localized delivery of chemotherapeutics.²³ For this, the biocompatibility and biodistribution of the MNHG was evaluated in Swiss mice, while efficacy in tumor growth inhibition was studied under the influence of an AC magnetic field (AMF). The *ex vivo* time-dependent pattern of accumulated MNHG in vital organs like lung, liver, spleen, kidney, and brain was also investigated. The tumor-bearing mice were subjected to hyperthermia by exposure to an RF magnetic field of 325 Oe operating at 265 kHz following intratumoral administration of dose I. The tumor size was measured at intervals of 72 h for a period of 2 weeks. The study revealed that the combinatorial therapy decelerated the growth of the tumor by ~ 3 -fold (size; $1,545 \pm 720 \text{ mm}^3$) as compared to the uninhibited exponential growth of the tumor (size; $4,510 \pm 735 \text{ mm}^3$) in control mice. These results clearly demonstrate that MNHGs have significant potential for use as platforms for combined thermo-chemotherapy.

T_c -tuned Magnetic Nanovesicles

Magnetic nanovesicles containing paclitaxel (**Sigma Prod. No. T7402**) and a dextran-coated biphasic suspension of $\text{La}_{0.75}\text{Sr}_{0.25}\text{MnO}_3$ and Fe_3O_4 magnetic nanoparticles were developed for use in chemotherapy and self-controlled (T_c tuned) hyperthermia.²⁴

Sequential release of paclitaxel at 37°C for 1 h followed by hyperthermic heating at 44°C for another 1 h (as expected for intratumoral injection) results in cumulative toxicity toward the cancer cells. **Figure 2** shows that under exposure to AMF, the temperature remains controlled at 44°C and a synergistic cytotoxicity of paclitaxel and hyperthermia is observed in MCF-7 cells. This indicates that magnetic nanovesicles containing biphasic suspension of $\text{La}_{0.75}\text{Sr}_{0.25}\text{MnO}_3$ and Fe_3O_4 nanoparticles encapsulating paclitaxel have potential for combined self-controlled hyperthermia and chemotherapy.

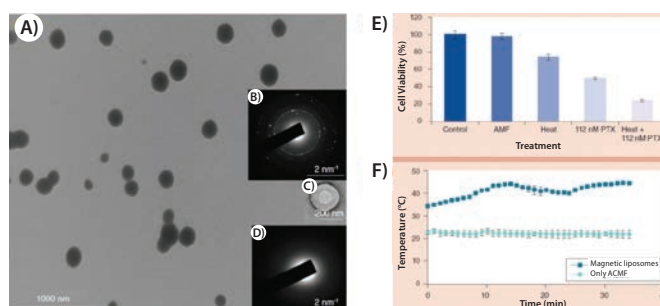


Figure 2. A) Transmission electron micrographs of magnetic liposomes containing biphasic suspension of $\text{La}_{0.75}\text{Sr}_{0.25}\text{MnO}_3$ and Fe_3O_4 nanoparticles in 10:1 ratio. Inset **(B, C, D)** shows the diffraction pattern of magnetic liposomes, transmission electron microscopy image of a blank liposome, and diffraction pattern of a blank liposome. **E)** Cellular toxicity of MCF-7 cell line during hyperthermia experiments. **F)** The temperature profile during the hyperthermia experiment, as well as only for the AC magnetic field.²⁴

Dendrimer-functionalized Magnetic Nanoparticles

Dendrimers are a class of hyper-branched symmetrical polymers that originate from a central core with repetitive branching units. Due to their structural properties and controlled size, dendrimers have emerged as an attractive material for biomedical applications, particularly as carriers for therapeutic cargos. Recently, there have been attempts to combine the unique features of dendrimer chemistry with the versatility of magnetic nanoparticles to provide a platform for enhanced therapeutics and biomedical applications.²⁵ For example, Rouhollah and co-workers combined magnetic nanoparticles with different generations of polyamidoamine (PAMAM) dendrimers (**Aldrich Prod. Nos. 664138** and **664049**) to develop pH-responsive platforms and deliver doxorubicin to resistant breast cancer (MCF-7) cells.²⁶ Yalcin and co-workers used PAMAM-coated magnetic nanoparticles to deliver the anticancer drug gemcitabine and retinoic acid to pancreatic cancer and stellate cells, successfully eliminating the cancer cells.²⁷ Boni and co-workers used amphiphilic PAMAM in combination with hydrophobic iron oxide nanoparticles to study relaxivity for MRI applications.²⁸ We recently developed dendrimer-conjugated iron oxide nanoparticles and explored the potential therapeutic efficiency of PAMAM- Fe_3O_4 -DOX triads.¹³ Different generations (G) (G3, G5, and G6) of PEG-PAMAMs were used to modify the surface of glutamic acid conjugated Fe_3O_4 nanoparticles (**Figure 3**). The biodistribution and biocompatibility of these DOX-loaded dendritic magnetic nanoparticles in C57BL/6 black mice are currently under investigation.

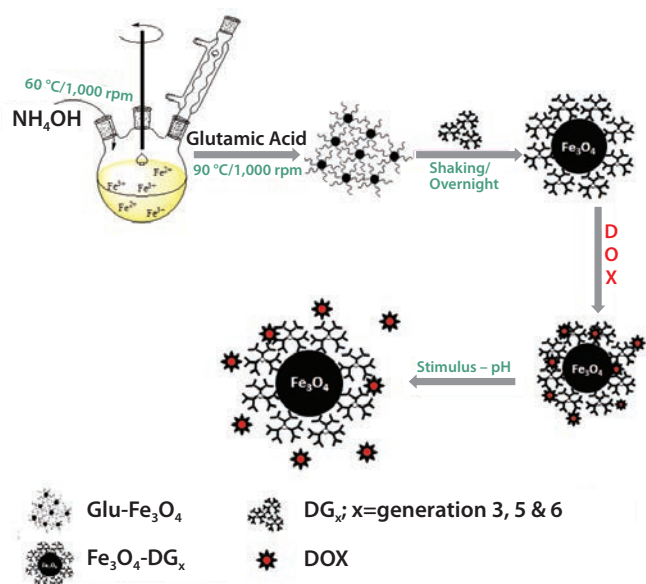


Figure 3. Illustration of the synthetic procedure for the synthesis of PAMAM- Fe_3O_4 -DOX triads and their application in pH-responsive drug delivery.¹³

Lipid-coated Mesoporous Magnetic Nanoassemblies

Lipid-based vesicles have attracted much interest in biomedical applications. Their tailorable composition, size, chemical properties, and ability to encapsulate drugs make lipids the first choice as delivery vectors. Results from Nappini and co-workers reveal that a low frequency alternating magnetic field can be utilized as the external stimuli to release drug molecules from lipid coated magnetic nanoparticles.²⁹ Park and co-workers have combined hyaluronic acid-based liposomes with commercially available magnevist as a platform for the delivery of doxorubicin to breast cancer cells and MRI of tumors.³⁰ In fact, the use of magnetic liposomes in gene delivery has also been reported. Recently, cholesterol and 1,2-distearoyl-sn-glycero-3-phosphocholine (DSPC)-based liposomes have been used by Jiang and co-workers to encapsulate iron oxide nanoparticles for the delivery of the gWiz-GFP plasmid DNA-encoding green fluorescent protein (GFP).³¹ A new pH- and thermo-sensitive drug delivery system consisting of a thin lipid (Sigma Prod. No. P0763) layer encapsulating mesoporous magnetite nanoassemblies (LMMNA) has been developed by our group (Figure 4). These LMMNAs are capable of carrying and delivering two anticancer drugs, namely hydrophilic doxorubicin hydrochloride (DOX) and hydrophobic paclitaxel (TXL), simultaneously.¹⁴ This hybrid system also acts as a heating platform when exposed to an AMF and exhibits a very high loading efficiency. The experiments reveal an improved *in vitro* cytotoxic effect when both drugs are delivered simultaneously in cervical cancer (HeLa), breast cancer (MCF-7), and liver cancer (HepG2) cells. The application of an AMF for 10 min substantially improves the cell killing efficiency due to the simultaneous thermo and chemotherapy.

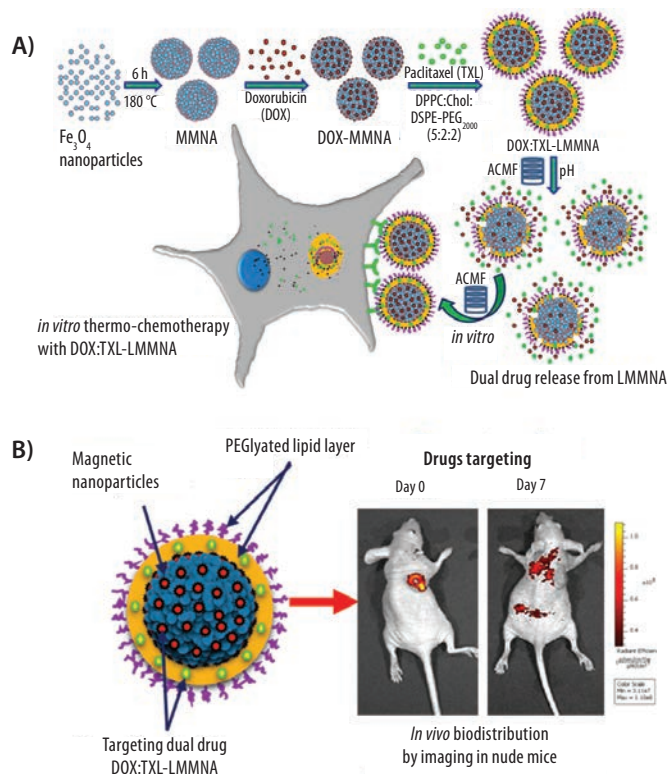


Figure 4. (A) Illustration of pH-sensitive and thermosensitive LMMNA as a dual drug delivery system containing doxorubicin (DOX) and paclitaxel (TXL). Drug release is triggered by an AC magnetic field applied to the tumor cells (B) *in vivo* biodistribution and thermo-chemotherapy studies controlled through fluorescence imaging.¹⁴

LMMNAs are currently under investigation as a dual drug delivery system for *in vivo* biodistribution and thermo-chemotherapy studies in subcutaneous tumor-bearing nude mice through fluorescence bioimaging. The biodistribution of these non-targeted nanoparticles is being studied in non-tumored nude mice by optical fluorescence imaging and measurement of Fe concentration in different vital organs. Biodistribution studies show a greater accumulation of lipid-coated magnetic nanoparticles in the large intestine, lung, liver, spleen, and stomach than in the kidney and heart. Tumor regression was also monitored by bioluminescence imaging as well as repeated fluorescence imaging due to the organ uptake of LMMNA-DOX:TXL. The combination therapy using an AC magnetic field with dual chemotherapeutics is currently under investigation in combating tumors in mice models.

Summary and Future Prospects

Multifunctional ferrofluids are one of the most intensively investigated functional nanomaterials for biomedical applications. The potential of external magnetic fields to manipulate the nanoparticles has enhanced their individual advantages in the direction of targeted chemotherapeutics, diagnostics and imaging of cancer. Multifunctionalized ferrofluids have been shown to offer improved cancer treatment and disease management. Research with multifunctional ferrofluids has moved forward from preliminary *in vitro* studies to a promising *in vivo* stage.

References

- (1) Cordova, G.; Attwood, S.; Gaikawad, R.; GuF; Leonenko, Z. *Nano Biomed. Eng.* **2014**, *6*, 31.
- (2) Hasany, S. F.; Abdurahman, N. H.; Sunarti, A. R.; Jose, R. *Current Nanoscience* **2013**, *9*, 561.
- (3) Xie, J.; Jon, S. *Theranostics* **2012**, *2*, 122.
- (4) Laurent, S.; Forge, D.; Port, M.; Roch, A.; Robic, C.; Elst, L. V.; Muller, R. N. *Chem. Rev.* **2008**, *108*, 2064.
- (5) Shokrollahi, H. *Materials Science and Engineering: C* **2013**, *33*, 2476–2487.
- (6) Chandra, S.; Barick, K. C.; Bahadur, D. *Advanced Drug Delivery Reviews* **2011**, *63*, 1267–1281.
- (7) Mornet, S.; Portier, J.; Duguet, E. *Journal of Magnetism and Magnetic Materials* **2005**, *293*, 127–134.
- (8) Hong, R. Y.; Pan, T. T.; Li, H. Z. *Journal of Magnetism and Magnetic Materials* **2006**, *303*, 60–68.
- (9) Rosensweig, R. E. *Journal of Magnetism and Magnetic Materials* **2002**, *252*, 370–374.
- (10) Laurent, S.; Dutz, S.; Häfeli, U. O.; Mahmoudi, M. *Advances in Colloid and Interface Science* **2011**, *166*, 8–23.
- (11) Love, R.; Soriano, R. Z.; Walsh, R. J. *Cancer Research* **1970**, *30*, 1525–1533.
- (12) Jordan, A.; Scholz, R.; Wust, P.; Fähling, H.; Roland, F. *Journal of Magnetism and Magnetic Materials* **1999**, *201*, 413–419.
- (13) Nigam, S.; Chandra, S.; Newgreen, D. F.; Bahadur, D.; Chen, Q. *Langmuir* **2014**, *30*, 1004–1011.
- (14) Pradhan, L.; Srivastava, R.; Bahadur, D. *Acta Biomaterialia* **2014**, *10*, 2976–2987.
- (15) Jaiswal, M. K.; Banerjee, R.; Pradhan, P.; Bahadur, D. *Colloids and Surfaces B: Biointerfaces* **2010**, *81*, 185–194.
- (16) Nigam, S.; Barick, K. C.; Bahadur, D. *Journal of Magnetism and Magnetic Materials* **2011**, *323*, 237–243.
- (17) Singh, N. S.; Hrishikesh, K.; Lina, P.; Bahadur, D. *Nanotechnology* **2013**, *24*, 065101.
- (18) Li, Y.; Huang, G.; Zhang, X.; Li, B.; Chen, Y.; Lu, T.; Lu, T. J.; Xu, F. *Advanced Functional Materials* **2013**, *23*, 660–672.
- (19) Lin, C.-W.; Tseng, S. J.; Kempson, I. M.; Yang, S.-C.; Hong, T.-M.; Yang, P.-C. *Biomaterials* **2013**, *34*, 4387–4393.
- (20) Zhang, D.; Sun, P.; Li, P.; Xue, A.; Zhang, X.; Zhang, H.; Jin, X. *Biomaterials* **2013**, *34*, 10258–10266.
- (21) Baeza, A.; Guisasaola, E.; Ruiz-Hernández, E.; Vallet-Regí, M. *Chemistry of Materials* **2012**, *24*, 517–524.
- (22) Jaiswal, M. K.; De, M.; Chou, S. S.; Vasavada, S.; Bleher, R.; Prasad, P. V.; Bahadur, D.; Dravid, V. P. *ACS Applied Materials & Interfaces* **2014**, *6*, 6237–6247.
- (23) Jaiswal, M. K.; Gogoi, M.; Dev Sarma, H.; Banerjee, R.; Bahadur, D. *Biomaterials Science* **2014**, *2*, 370–380.
- (24) Gogoi, M.; Sarma, H. D.; Bahadur, D.; Banerjee, R. *Nanomedicine* **2013**, *9*, 955–970.
- (25) Chandra, S.; Nigam, S.; Bahadur, D. *Journal of Biomedical Nanotechnology* **2014**, *10*, 32–49.
- (26) Rouhollah, K.; Pelin, M.; Serap, Y.; Gozde, U.; Ufuk, G. *Journal of Pharmaceutical Sciences* **2013**, *102*, 1825–1835.
- (27) Yalçın, S.; Erkan, M.; Ünsoy, G.; Parsian, M.; Kleeff, J.; Gündüz, U. *Biomedicine & Pharmacotherapy* **2014**, *68*, 737–743.
- (28) Boni, A.; Albertazzi, L.; Innocenti, C.; Gemmi, M.; Bifone, A. *Langmuir* **2013**, *29*, 10973–10979.
- (29) Nappini, S.; Bonini, M.; Bombelli, F. B.; Pineider, F.; Sangregorio, C.; Baglioni, P.; Norden, B. *Soft Matter* **2011**, *7*, 1025–1037.
- (30) Park, J.-H.; Cho, H.-J.; Yoon, H. Y.; Yoon, I.-S.; Ko, S.-H.; Shim, J.-S.; Cho, J.-H.; Park, J. H.; Kim, K.; Kwon, I. C.; Kim, D.-D. *Journal of Controlled Release* **2014**, *174*, 98–108.
- (31) Jiang, S.; Eltoukhy, A. A.; Love, K. T.; Langer, R.; Anderson, D. G. *Nano Letters* **2013**, *13*, 1059–1064.

Nanomaterials for Biomedical Applications

Gold Nanoparticles (Dispersions in H₂O; OD=50)

For a complete list of available materials, visit aldrich.com/goldnanomaterials.

Surface	Dimension	Prod. No.	
amine functionalized, PEG 3000 coated	diameter 5 nm	765260-1ML	
	diameter 10 nm	765295-1ML	
	diameter 15 nm	765317-1ML	
	diameter 20 nm	765333-1ML	
	diameter 30 nm	765368-1ML	
	diameter 40 nm	765384-1ML	
amine functionalized, PEG 5000 coated	diameter 10 nm	765309-1ML	
	diameter 15 nm	765325-1ML	
	diameter 20 nm	765341-1ML	
	diameter 30 nm	765376-1ML	
	diameter 40 nm	765392-1ML	
	carboxylic acid functionalized, PEG 3000 coated	diameter 10 nm	765457-1ML
diameter 20 nm		765503-1ML	
diameter 40 nm		765554-1ML	
diameter 50 nm		765570-1ML	
carboxylic acid functionalized, PEG 5000 coated		diameter 5 nm	765449-1ML
		diameter 10 nm	765465-1ML
	diameter 30 nm	765546-1ML	
	diameter 40 nm	765562-1ML	
	diameter 50 nm	765589-1ML	
	methyl terminated, PEG 2000 coated	diameter 5 nm	765597-1ML
diameter 10 nm		765619-1ML	
diameter 15 nm		765694-1ML	
diameter 20 nm		765716-1ML	
diameter 30 nm		765635-1ML	
diameter 40 nm		765651-1ML	
methyl terminated, PEG 5000 coated	diameter 50 nm	765678-1ML	
	diameter 5 nm	765600-1ML	
	diameter 10 nm	765627-1ML	
	diameter 20 nm	765724-1ML	
	diameter 30 nm	765732-1ML	
	diameter 40 nm	765643-1ML	
	diameter 50 nm	765686-1ML	

Silver Nanoparticles

For a complete list of available materials, visit aldrich.com/nanopowders.

Description	Concentration	Dimension	Prod. No.
PVP functionalized	0.02 mg/mL in water	avg. part. size 10 nm	795925-25ML
	0.02 mg/mL in water	avg. part. size 20 nm	795933-25ML
	0.02 mg/mL in water	avg. part. size 30 nm	795941-25ML
	0.02 mg/mL in water	avg. part. size 40 nm	795968-25ML
	0.02 mg/mL in water	avg. part. size 50 nm	795976-25ML
	0.02 mg/mL in water	avg. part. size 60 nm	795984-25ML
	0.02 mg/mL in water	avg. part. size 80 nm	795992-25ML
	0.02 mg/mL in water	avg. part. size 200 nm	796026-25ML

Iron Oxide (Fe₃O₄) Nanoparticles

For a complete list of available materials, visit aldrich.com/nanopowders.

Functional Group	Concentration	Form	Dimension	Prod. No.
amine	Fe 1 mg/mL	dispersion in H ₂ O	diameter 5 nm particle size 4 - 6 nm (TEM)	747343-10ML
	Fe 1 mg/mL	dispersion in H ₂ O	diameter 10 nm particle size 9 - 11 nm (TEM)	747300-10ML
	Fe 1 mg/mL	dispersion in H ₂ O	diameter 30 nm particle size 28 - 32 nm (TEM)	747327-10ML
biotin	Fe 1 mg/mL	dispersion in H ₂ O	diameter 5 nm particle size 4 - 6 nm (TEM)	747416-1ML
	Fe 1 mg/mL	dispersion in H ₂ O	diameter 10 nm particle size 9 - 11 nm (TEM)	747424-1ML
	Fe 1 mg/mL	dispersion in H ₂ O	diameter 30 nm particle size 28 - 32 nm (TEM)	747432-1ML
carboxylic acid	Fe 5 mg/mL	dispersion in H ₂ O	diameter 10 nm particle size 9 - 11 nm (TEM)	747254-2ML
	Fe 5 mg/mL	dispersion in H ₂ O	diameter 30 nm particle size 28 - 32 nm (TEM)	747335-2ML
PEG	Fe 1 mg/mL	dispersion in H ₂ O	diameter 5 nm particle size 4 - 6 nm (TEM)	790508-10ML
	Fe 1 mg/mL	dispersion in H ₂ O	diameter 10 nm particle size 9 - 11 nm (TEM)	747319-10ML
	Fe 1 mg/mL	dispersion in H ₂ O	diameter 30 nm particle size 28 - 32 nm (TEM)	747408-10ML
N-succinimidyl ester	-	powder	diameter 5 nm particle size 4 - 6 nm (TEM)	747440-1G
	-	powder	diameter 10 nm particle size 9 - 11 nm (TEM)	747459-1G
	-	powder	diameter 30 nm particle size 28 - 32 nm (TEM)	747467-1G

Mesoporous Silica

For a complete list of available materials, visit aldrich.com/mesoporous.

Name	Pore Size (nm)	Dimension	Prod. No.
Propylcarboxylic acid functionalized silica	4	particle size 200 nm	749664-1G 749664-5G
		particle size 200 nm	749710-1G
Propylthiol functionalized silica	4	particle size 200 nm	749362-1G 749362-5G
		particle size 200 nm	748161-1G 748161-5G

MATERIALS FOR INNOVATION



BIOMEDICAL

Materials for drug delivery, tissue engineering, and regenerative medicine; PEGs, biodegradable and natural polymers; functionalized nanoparticles; block copolymers, dendrimers and nanoclays

ELECTRONICS

Nanowires; printed electronics inks and pastes; materials for OPV, OFET, OLED; nanodispersions; CNTs and graphene; precursors for PVD, CVD, and sputtering

ENERGY

Ready-to-use battery grade electrode and electrolyte materials; nanopowders, nanostructures and dispersions; quantum dots; perovskites; fuel cells and membrane; hydrogen storage materials including MOFs; phosphors; thermoelectrics; high purity salts

Find more information on our capabilities at
aldrich.com/matsci